

Gallium Anomaly: Critical View from the Global Picture of ν_e and $\bar{\nu}_e$ Disappearance

C. Giunti,^{1,*} Y.F. Li,^{2,3,†} C.A. Ternes,^{1,4,‡} O. Tyagi,^{1,5,§} and Z. Xin^{2,3,¶}

¹*Istituto Nazionale di Fisica Nucleare (INFN), Sezione di Torino, Via P. Giuria 1, I-10125 Torino, Italy*

²*Institute of High Energy Physics, Chinese Academy of Sciences, Beijing 100049, China*

³*School of Physical Sciences, University of Chinese Academy of Sciences, Beijing 100049, China*

⁴*Dipartimento di Fisica, Università di Torino, via P. Giuria 1, I-10125 Torino, Italy*

⁵*School of Physical Sciences, Jawaharlal Nehru University, New Delhi 110067, India*

(Dated: Wednesday 02/11/22, 00:54)

The significance of the Gallium Anomaly, from the BEST, GALLEX, and SAGE radioactive source experiments, is quantified using different theoretical calculations of the neutrino detection cross section, and its explanation due to neutrino oscillations is compared with the bounds from the analyses of reactor rate and spectral ratio data, β -decay data, and solar neutrino data. In the 3+1 active-sterile neutrino mixing scheme, the Gallium Anomaly is in strong tension with the individual and combined bounds of these data sets. In the combined scenario with all available data, the parameter goodness of fit is below 0.042%, corresponding to a severe tension of 4–5 σ , or stronger. Therefore, we conclude that one should pursue other possible solutions beyond short-baseline oscillations for the Gallium Anomaly. We also present a new global fit of ν_e and $\bar{\nu}_e$ disappearance data, showing that there is a 2.6–3.3 σ preference in favor of short-baseline oscillations, which is driven by an updated analysis of reactor spectral ratio data.

Contents

I. Introduction	1
II. The Gallium Anomaly	2
III. The reactor rates constraints	4
IV. Short-baseline reactor spectral ratios	5
V. Combined short-baseline reactor spectral ratios and rates	6
VI. The KATRIN limit	8
VII. Combination of short-baseline reactor data and Tritium constraints	11
VIII. The solar neutrino bound	13
IX. Global ν_e and $\bar{\nu}_e$ disappearance analysis	15
X. Summary and conclusions	17
References	19

I. Introduction

The possible existence of light sterile neutrinos is a hot topic of current research in high-energy physics.

It was motivated by anomalies found in short-baseline neutrino oscillation experiments: the Gallium Anomaly, the Reactor Antineutrino Anomaly, and the LSND and MiniBooNE anomalies (see the reviews in Refs. [1–6]). Most puzzling is the large Gallium Anomaly, which has been recently revived by the results of the BEST experiment [7, 8]. In this paper we discuss the status of short-baseline ν_e and $\bar{\nu}_e$ disappearance and we compare the neutrino oscillation explanation of the Gallium Anomaly with the constraints from other experiments.

The standard paradigm in the phenomenology of massive neutrinos is the three-neutrino mixing scheme in which the three well known active flavor neutrinos ν_e , ν_μ , and ν_τ take part in the weak interactions of the Standard Model and are unitary superpositions of three massive neutrinos ν_1 , ν_2 , and ν_3 with respective masses m_1 , m_2 , and m_3 . The two independent squared-mass differences $\Delta m_{21}^2 \approx 7.4 \times 10^{-5} \text{ eV}^2$ and $|\Delta m_{31}^2| \approx 2.5 \times 10^{-3} \text{ eV}^2$ (with $\Delta m_{kj}^2 \equiv m_k^2 - m_j^2$) generate the oscillations observed in solar, atmospheric and long-baseline neutrino oscillation experiments (see e.g., Ref. [9] and the recent three-neutrino global analyses in Refs. [10–12]). Short-baseline (SBL) oscillations that could explain the Reactor Antineutrino Anomaly and the Gallium Anomaly require the existence of at least one additional squared-mass difference $\Delta m_{\text{SBL}}^2 \gtrsim 1 \text{ eV}^2$. In the minimal 3+1 scenario that we consider here there is a non-standard massive neutrino ν_4 with mass $m_4 \gtrsim 1 \text{ eV}$ which generates the short-baseline squared-mass difference $\Delta m_{\text{SBL}}^2 \simeq \Delta m_{41}^2$. In the flavor basis, the new neutrino corresponds to a sterile neutrino ν_s which does not take part in the weak interactions of the Standard Model (see the reviews in Refs. [1–6]). In this framework, the effective short-baseline survival probability of electron neutrinos and antineutrinos relevant for reactor and Gallium ex-

* carlo.giunti@to.infn.it

† liyufeng@ihep.ac.cn

‡ ternes@to.infn.it

§ oddhar89_sps@jnu.ac.in

¶ xinzhaoh@ihep.ac.cn

periments is given by

$$P_{ee} \simeq 1 - \sin^2 2\vartheta_{ee} \sin^2 \left(\frac{\Delta m_{41}^2 L}{4E} \right). \quad (1)$$

The effective mixing angle ϑ_{ee} depends on the element U_{e4} of the 4×4 mixing matrix U through the relation $\sin^2 2\vartheta_{ee} = 4|U_{e4}|^2(1 - |U_{e4}|^2)$.

Currently, the Reactor Antineutrino Anomaly is regarded to be resolved or, at least, diminished with the new refinements of reactor flux models [13, 14], but the Gallium Anomaly is reinforced by the new measurements of the BEST experiment [7, 8]. Therefore, it is desirable to pay special attention to the Gallium Anomaly, and look for possible viable solutions. In this work, we first evaluate the statistical significance of the Gallium Anomaly with different calculations of the neutrino detection cross section. Then, we compare the neutrino oscillation explanation of the Gallium Anomaly with the bounds from several classes of ν_e and $\bar{\nu}_e$ disappearance experiments. In particular, we compare it with the above mentioned Reactor Antineutrino Anomaly and also with the results of an updated analysis of reactor spectral ratio data. Interestingly, the preference for short-baseline neutrino oscillations is reinforced when considering the newest spectral ratio data, as will be detailed below. We also consider data from tritium experiments and from experiments measuring solar neutrinos, before combining all data to a global ν_e and $\bar{\nu}_e$ disappearance fit. The consistency of a solution of the Gallium Anomaly with 3+1 active-sterile neutrino mixing will be compared and discussed at each step.

This work is organized as follows. In Section II, we discuss the analysis of Gallium data for several cross section models and we quantify the significance of the Gallium Anomaly. In Sections III and IV we compare the results of the Gallium experiments with those obtained from the analysis of reactor rate and spectral ratio data, respectively. Section V contains the combined analysis of all reactor data. In Section VI we detail the analysis procedure for the KATRIN data, and in Section VII we discuss the comparison of the regions of parameter space preferred by KATRIN and other β -decay experiments in combination with reactor data with those preferred by the Gallium data. Section VIII discusses the updated solar neutrino bounds. Finally, in Section IX we combine all the data discussed in previous sections to a global 3+1 ν_e and $\bar{\nu}_e$ disappearance fit and we compare the results with those obtained from the Gallium data. We close with a discussion and a summary of our results in Section X.

II. The Gallium Anomaly

The Gallium Anomaly was originally [20–22] a deficit of events observed in the GALLEX [23–25] and SAGE [20, 26–28] source experiments aimed at testing the solar neutrino detection done in these experiments

through the process $\nu_e + {}^{71}\text{Ga} \rightarrow e^- + {}^{71}\text{Ge}$. Two source experiments have been done by the GALLEX collaboration using an intense artificial ${}^{51}\text{Cr}$ radioactive source placed inside the detector. This source emitted electron neutrinos through the electron capture (EC) process $e^- + {}^{51}\text{Cr} \rightarrow {}^{51}\text{V} + \nu_e$. The SAGE collaboration performed a source experiment with a ${}^{51}\text{Cr}$ radioactive source and another with a ${}^{37}\text{Ar}$ radioactive source, which emitted electron neutrinos through the EC process $e^- + {}^{37}\text{Ar} \rightarrow {}^{37}\text{Cl} + \nu_e$. The deficits of the observed rates with respect to the rates calculated from the well-measured activity of the sources and different cross sections for the detection process (see Tab. I) have been discussed in many papers (see the reviews in Refs. [1–6]). The deficits obtained using the earliest Bahcall cross section [16] are illustrated in Fig. 1(a), where we plotted the ratios of observed and predicted rates versus the average path lengths of the neutrinos (about 1.9 m for GALLEX and 0.6 m for SAGE). The figure shows also the results of the recent BEST source experiment [7, 8], where a larger deficit was observed, confirming the Gallium Anomaly. The two BEST values in Fig. 1(a) show the ratio of observed and predicted rates in the two nested ${}^{71}\text{Ga}$ volumes of the experiment, which correspond to average neutrino path lengths of about 0.5 m and 1.1 m [7, 8]. Although the ratios shown in Fig. 1(a) exhibit some variation with distance, we cannot see a clear oscillatory behavior. Taking into account the large error bars and a 2.8% correlated systematic uncertainty of the Bahcall cross section, the data can be fitted with a constant average ratio $\bar{R} = 0.80 \pm 0.04$. We considered the systematic uncertainty of the ${}^{51}\text{Cr}$ cross section as correlated among all the experiments and we added in quadrature the small residual systematic uncertainty of the ${}^{37}\text{Ar}$ cross section to the uncertainty of the SAGE ${}^{37}\text{Ar}$ measurement.

From the absence of a clear oscillatory pattern as a function of distance in Fig. 1(a) and, in particular, the quasi-equality of the two BEST measurements at different distances, it follows that there is no smoking-gun evidence of oscillations in the Gallium data. After the BEST measurements, the Gallium Anomaly is still an anomaly based on the absolute comparison of observed and predicted rates, as it was when only the GALLEX and SAGE data were available. Therefore, a crucial role is played by the theoretical detection cross section, for which there are the different model calculations listed in Tab. I. The difference between these cross section models is the contribution to the cross section coming from the transitions from the ground state of ${}^{71}\text{Ga}$ to excited states of ${}^{71}\text{Ge}$. As shown in the first line of Tab. I, the ground-state to ground-state cross section is known with a very small uncertainty from the measured lifetime of ${}^{71}\text{Ge}$ [16]. The table shows the relative contributions δ_{exc} of the transitions to the excited states in the different calculations of the cross section. These relative contributions vary from about 2-3% in the Shell Model calculation of Kostensalo et al. [19] to about 13-14% in the Shell Model calculation of Haxton [17].

Model	Method	^{51}Cr		^{37}Ar		\bar{R}	GA
		σ_{tot}	δ_{exc}	σ_{tot}	δ_{exc}		
Ground State [15]	$T_{1/2}(^{71}\text{Ge})$	5.539 ± 0.019	—	6.625 ± 0.023	—	0.844 ± 0.031	5.0σ
Bahcall (1997) [16]	$^{71}\text{Ga}(p, n)^{71}\text{Ge}$	5.81 ± 0.16	4.7%	7.00 ± 0.21	5.4%	0.802 ± 0.037	5.4σ
Haxton (1998) [17]	Shell Model	6.39 ± 0.65	13.3%	7.72 ± 0.81	14.2%	0.703 ± 0.078	3.8σ
Frekers et al. (2015) [18]	$^{71}\text{Ga}(^3\text{He}, ^3\text{H})^{71}\text{Ge}$	5.92 ± 0.11	6.4%	7.15 ± 0.14	7.3%	0.788 ± 0.032	6.5σ
Kostensalo et al. (2019) [19]	Shell Model	5.67 ± 0.06	2.3%	6.80 ± 0.08	2.6%	0.824 ± 0.031	5.6σ
Semenov (2020) [15]	$^{71}\text{Ga}(^3\text{He}, ^3\text{H})^{71}\text{Ge}$	5.938 ± 0.116	6.7%	7.169 ± 0.147	7.6%	0.786 ± 0.033	6.6σ

TABLE I. $\nu_e + ^{71}\text{Ga} \rightarrow ^{71}\text{Ge} + e^-$ cross sections in units of 10^{-45} cm^2 and the corresponding relative contributions δ_{exc} of the transitions to the excited states. Also shown are the average ratio \bar{R} of observed and predicted events and the statistical significance of the corresponding Gallium Anomaly.

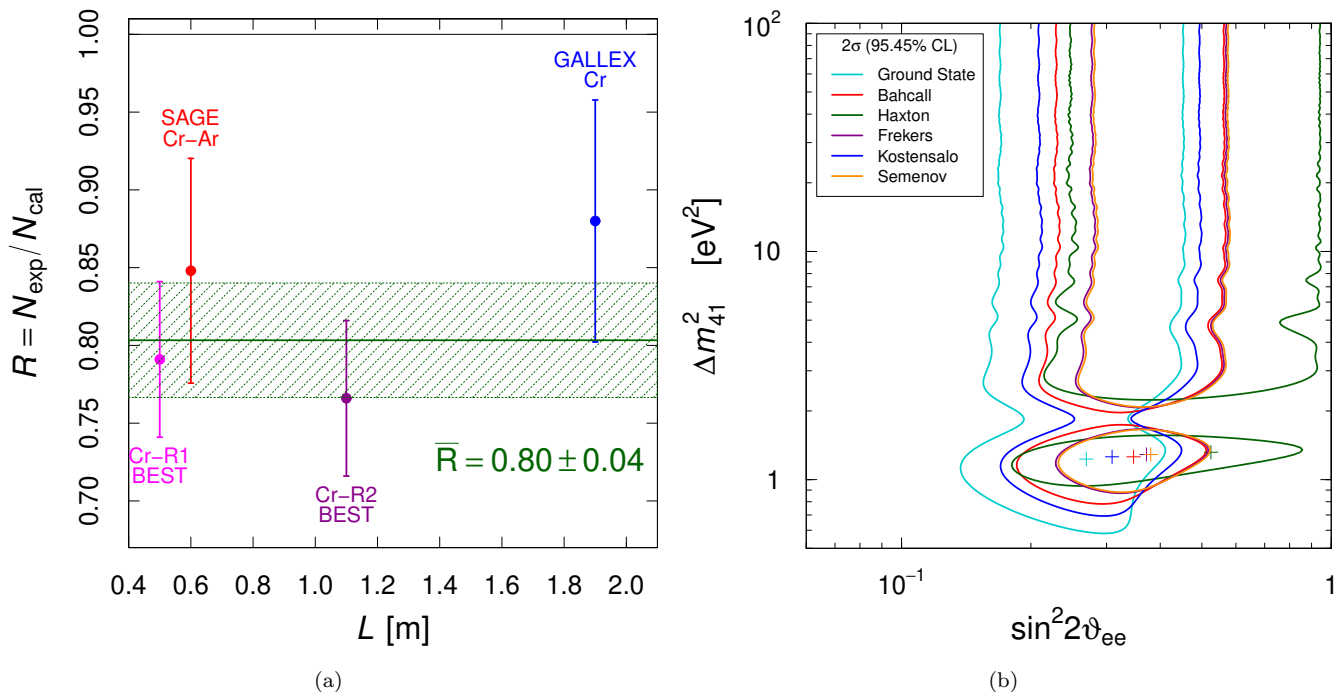


FIG. 1. (a) Ratios of observed and predicted event rates in the Gallium source experiments obtained using the Bahcall cross sections [16]. (b) Contours enclosing the 2σ allowed regions in the $(\sin^2 2\vartheta_{ee}, \Delta m_{41}^2)$ plane obtained from the Gallium data with the different cross sections in Tab. I. The best-fit points are indicated by crosses. Note that the Frekers (magenta) and Semenov (orange) contours are almost superimposed.

Table I shows also the values of the average ratio \bar{R} of observed and predicted events obtained with the different cross section models and the statistical significance of the corresponding Gallium Anomaly. One can see that the statistical significance of the Gallium Anomaly is large, about 5-6 σ , for all the cross section models, except for the Haxton cross section model, because of its large uncertainties, in spite of the larger Haxton cross sections. Let us however note that the Shell Model cross section of Haxton [17], calculated in 1998, should be considered as superseded by the more recent Shell Model cross section of Kostensalo et al. [19], which was calculated in 2019 using a state-of-the-art code and recently developed two-nucleon interactions.

In the first line of Tab. I (Ground State model) we con-

sidered the possibility that the cross section is dominated by the transition to the ground state of ^{71}Ge , with negligible contributions of the transitions to the excited states of ^{71}Ge . The value of the Ground State cross section is taken from the recent estimate in Ref. [15]. This is an extreme possibility that is justified by the reliability of the cross section to the ground state of ^{71}Ge discussed above and by the uncertainties of the cross sections to the excited states of ^{71}Ge , which depend on the methods and assumptions of the different models. The Ground State model corresponds to the minimum possible value of the cross section and gives the maximum possible value of the average ratio \bar{R} of observed and predicted events. As one can see from Tab. I, even in this extreme case the value of \bar{R} is 5.0σ below one. This is a strong signal of

the seriousness of the Gallium Anomaly.

The Gallium Anomaly can be explained by short-baseline neutrino oscillations in the 3+1 active-sterile neutrino mixing framework described briefly in Section I. Fig. 1(b) shows the 2σ allowed regions in the $(\sin^2 2\vartheta_{ee}, \Delta m_{41}^2)$ plane obtained from the analyses of the Gallium data with the different cross sections in Tab. I. One can see that in all cases there is a clear indication of a relatively large value of $\sin^2 2\vartheta_{ee}$ for $\Delta m_{41}^2 \gtrsim 0.6 \text{ eV}^2$. The minimum 2σ value of $\sin^2 2\vartheta_{ee}$ is about 0.14 in the case of the Ground State model. This large value of $\sin^2 2\vartheta_{ee}$ is required to produce an oscillation amplitude that is sufficient to explain the deficit represented by the Ground State value of \bar{R} in Tab. I at the 2σ level. The smaller values of \bar{R} for the other cross section models correspond to allowed regions that cover larger values of $\sin^2 2\vartheta_{ee}$. The Kostensalo Shell Model cross section requires values of $\sin^2 2\vartheta_{ee}$ that are only slightly larger than those of the Ground State cross section, $\sin^2 2\vartheta_{ee} \gtrsim 0.17$, because of the small contribution of the transitions to the excited states of ^{71}Ge in this cross section model. The older Shell Model cross section of Haxton, which has much larger contributions of the transitions to the excited states of ^{71}Ge , gives a broad allowed region that spans values of $\sin^2 2\vartheta_{ee}$ from about 0.18 to about 0.95, because of the large cross section uncertainties shown in Tab. I. The Bahcall cross section implies $\sin^2 2\vartheta_{ee} \gtrsim 0.17$, and the almost-equal Frekers and Semenov cross sections give $\sin^2 2\vartheta_{ee} \gtrsim 0.23$. Our results on the significance of the Gallium anomaly are in reasonable agreement with the results obtained in Ref. [29].

In the following, when we will compare the Gallium Anomaly with the results of other experiments, we will consider only the following four cross section models:

Ground State: This is a significant extreme case as discussed above.

Bahcall: It is the first and most used cross section model [16].

Kostensalo: It is the most recent Shell Model calculation [19], which supersedes the much older Haxton calculation [17], as discussed above.

Semenov: It is a recent [15] reevaluation of the cross sections which uses the $^{71}\text{Ga}(^3\text{He}, ^3\text{H})^{71}\text{Ge}$ data of Frekers et al. [18] and supersedes their evaluation of the cross section.

III. The reactor rates constraints

The phenomenology of reactor neutrinos focused on the Reactor Antineutrino Anomaly in 2011 [30], after the reevaluations of the predicted reactor antineutrino fluxes by Mueller *et al.* [31] and Huber [32] (HM model), which led to a deficit of about 2.5σ of observed event rates in short-baseline reactor neutrino experiments with

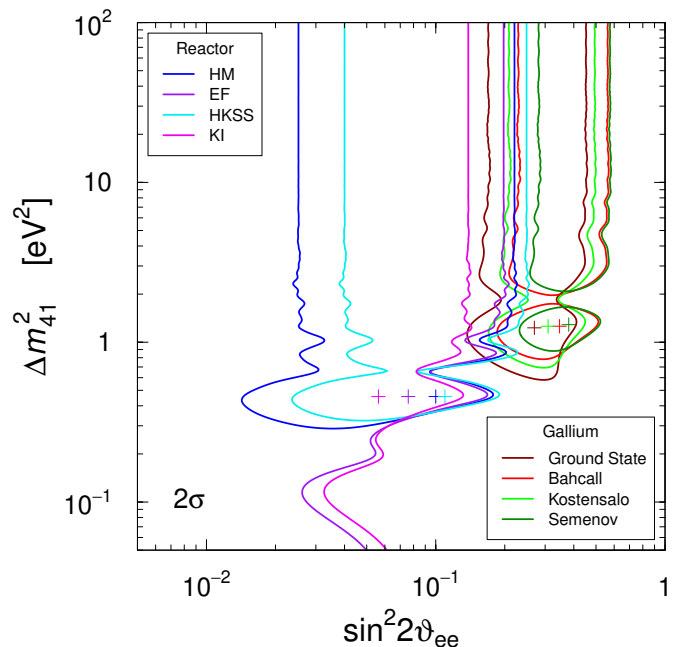


FIG. 2. Contours delimiting the 2σ allowed regions in the $(\sin^2 2\vartheta_{ee}, \Delta m_{41}^2)$ plane obtained from the Gallium data with different cross sections compared with those obtained in Ref. [14] from the analysis of short-baseline reactor rate data. The best-fit points are indicated by crosses.

respect to the predictions. Recent theoretical and experimental developments led to new reactor flux models with enhanced (HKSS model of Hayen, Kostensalo, Severijns, and Suhonen [33]) or diminished (EF model of Estienne, Fallot *et al.* [34] and KI model of Kopeikin *et al.* [35]) Reactor Antineutrino Anomaly. In particular, the EF and KI flux models give average ratios of observed and predicted events that are only about 1σ smaller than unity, hinting at the demise of the Reactor Antineutrino Anomaly [13, 14]. Here we use the results of the analysis in Ref. [14], where it was shown that all the reactor flux models imply upper bounds for the 3+1 active-sterile neutrino mixing parameter $\sin^2 2\vartheta_{ee}$ that are smaller than about 0.25 at 2σ . This bound is in tension with the large values of $\sin^2 2\vartheta_{ee}$ which are required to explain the Gallium Anomaly, as discussed in Section II.

Figure 2 shows a comparison of the 2σ allowed regions in the $(\sin^2 2\vartheta_{ee}, \Delta m_{41}^2)$ plane obtained from the analyses of reactor rates and Gallium data. One can see that there is only a small overlap of the reactor and Gallium regions for some models. The largest overlaps occur for the Ground State Gallium cross section model, whose allowed region extends to the smallest values of $\sin^2 2\vartheta_{ee}$ allowed by the Gallium Anomaly, and for the HKSS reactor flux model, which gives the largest Reactor Antineutrino Anomaly.

Table II shows the χ^2 difference $\Delta\chi_{\text{PG}}^2$ of the parameter goodness of fit test [36] between the reactor rates and the Gallium data corresponding to the models in Fig. 2. Table II shows also the corresponding values of

	HM		HKSS		EF		KI	
	$\Delta\chi_{\text{PG}}^2$	GoF _{PG}						
Ground State	7.2	2.8%	5.4	6.8%	9.1	1.1%	11.9	0.26%
Bahcall	10.9	0.42%	8.9	1.2%	12.9	0.16%	16.3	0.029%
Kostensalo	9.6	0.83%	7.5	2.4%	11.5	0.31%	15.3	0.049%
Semenov	15.1	0.052%	12.6	0.18%	17.0	0.02%	22.5	0.0013%

TABLE II. χ^2 difference $\Delta\chi_{\text{PG}}^2$ of the parameter goodness of fit test [36] between the reactor rate data and the Gallium data corresponding to four different reactor flux predictions (HM, HKSS, EF, and KI) discussed in the text and four of the different Gallium detection cross sections in Tab. I. The values of the corresponding parameter goodness of fit GoF_{PG} are calculated with two degrees of freedom corresponding to the two oscillation parameters $\sin^2 2\theta_{ee}$ and Δm_{41}^2 which are common in the reactor rates and Gallium data analyses.

the parameter goodness of fit GoF_{PG}, which quantifies the tension between the fits of reactor rates and Gallium data in the different models. Considering the extreme case of Ground State Gallium cross section model, the largest tension is obtained with the KI reactor flux model (GoF_{PG} = 0.26%). Indeed, one can see from Fig. 2 that the corresponding 2σ allowed regions have only a very marginal overlap for $\Delta m_{41}^2 \simeq 1 \text{ eV}^2$.

The more realistic Bahcall, Kostensalo, and Semenov cross section models give larger tensions between the reactor rates and Gallium data. If we consider as severe a tension with a GoF_{PG} smaller than 1%, for the Bahcall and Kostensalo cross section models there is a severe tension between Gallium data and reactor rates for all reactor flux models, except the HKSS model, while for the Semenov cross section model there is a severe tension for all of the reactor flux models. One can also notice that the KI reactor flux model gives the maximal tension for all Gallium cross section models and it is always severe. The EF reactor flux model gives a severe tension for all the Gallium cross section models, except for the Ground State model, where it is a marginal 1.1%.

Since the EF and KI reactor flux models are those that may have solved the Reactor Antineutrino Anomaly [13, 14, 29] and are currently believed to represent reliable replacements of the standard HM model, we conclude that the tension between Gallium data and reactor rates is a serious issue in the framework of 3+1 active-sterile neutrino oscillations.

Let us also emphasize that extending the 3+1 model with the introduction of more sterile neutrinos does not help, because any disappearance of neutrinos in Gallium experiments must correspond to an antineutrino disappearance of the same size in reactor experiments. A possible loophole is a violation of the CPT symmetry [37], which implies the equality of the disappearance probabilities of neutrinos and antineutrinos (see, e.g., Ref. [38]). Although this loophole may resolve the tension between the Gallium neutrino data and reactor antineutrino rates, it cannot explain the tension between the Gallium neutrino data and the solar neutrino bound discussed in Section VIII.

IV. Short-baseline reactor spectral ratios

Short-baseline oscillations of reactor antineutrinos can be probed in a model-independent way by comparing the rates or spectra measured at different distances from the reactor antineutrino source. This is the approach adopted by the recent DANSS [39, 40], PROSPECT [41, 42], and STEREO [43, 44] experiments. Important results have been obtained also by the NEOS collaboration [45] and by a joint analysis of the RENO and NEOS collaborations [46]. In 2017 [45] the NEOS collaboration published the results of the comparison of NEOS data at about 24 m from the reactor source with the prediction obtained from the neutrino flux measured in the Daya Bay experiment [47] at a distance of about 550 m from the reactor source, where the short-baseline oscillations are averaged. Recently, the RENO and NEOS collaborations published a joint paper [46] with the results of the comparison of NEOS data with the prediction obtained from the neutrino flux measured in the RENO experiment at a distance of about 419 m from the reactor source, which is in the same reactor complex of NEOS. This comparison allowed the RENO and NEOS collaborations to reduce the systematic uncertainties with respect to the NEOS/Daya Bay analysis.

In the following we consider both the NEOS/Daya Bay and NEOS/RENO data, because it is obviously unknown which one of the Daya Bay and RENO neutrino spectra is more accurate. For NEOS/Daya Bay we use the χ^2 table kindly provided by the NEOS collaboration, as already done in Refs. [48–51]. For NEOS/RENO we performed a fit using the information in the data release of Ref. [46]. We verified that our fit reproduces with good approximation the results published in Ref. [46]. For the DANSS experiment we use the χ^2 table kindly provided by the DANSS collaboration, which corresponds to the latest results presented at the recent ICHEP 2022 conference [40]. For the PROSPECT experiment we performed a fit using the information in the data release of Ref. [42]. For the STEREO experiment we use the χ^2 table in the data release of Ref. [44].

In this analysis we do not consider the controversial results of the Neutrino-4 experiment: the Neutrino-4 col-

laboration claimed a 2.9σ evidence of short-baseline neutrino oscillations with large mixing ($\sin^2 2\vartheta_{ee} = 0.36 \pm 0.12$) at $\Delta m_{41}^2 = 7.3 \pm 1.17$ [52]. However, these results were criticized in Refs. [53–56]. In particular, the energy resolution of the detector was not taken into account in the analysis of the Neutrino-4 collaboration, as it is clear from a sentence in Ref. [52], where they confuse energy binning with taking into account the energy resolution of the detector. A combined analysis of spectral ratio data including Neutrino-4 (but not the latest DANSS data) has been performed in Ref. [29].

Figure 3 shows the allowed regions in the $(\sin^2 2\vartheta_{ee}, \Delta m_{41}^2)$ plane obtained from the combined analysis of the NEOS/Daya Bay or NEOS/RENO spectral ratio data with those of the other experiments. For completeness, besides the data of the recent DANSS [40], PROSPECT [42], and STEREO [44] experiments mentioned above, we considered also the 40/50 m spectral ratio data of the old Bugey-3 experiment [57], as already done in Refs. [48–51]. Figure 3 shows also the contours of the 2σ allowed regions of each experiments. One can see that at 2σ PROSPECT, STEREO, and Bugey-3 produce only exclusion curves, whereas NEOS/Daya Bay, NEOS/RENO, and DANSS yield closed contours.

The result of the combined fit is different when we consider NEOS/Daya Bay or NEOS/RENO. The combined fit with NEOS/Daya Bay (Fig. 3(a)) results in a 3.1σ indication in favor of short-baseline oscillations with best-fit parameters values $\sin^2 2\vartheta_{ee} = 0.022$ and $\Delta m_{41}^2 = 1.29 \text{ eV}^2$. One can see that the surrounding region is the locus of a remarkable overlap of relatively large 2σ allowed regions of NEOS/Daya Bay and DANSS, which are not excluded by the 2σ exclusion curves of PROSPECT, STEREO, and Bugey-3. In the combined fit with NEOS/RENO (Fig. 3(b)), the best-fit is approximately the same, $\sin^2 2\vartheta_{ee} = 0.017$ and $\Delta m_{41}^2 = 1.32 \text{ eV}^2$, but the indication in favor of short-baseline oscillations is only of 2.6σ . Therefore, in Fig. 3(b) the combined 3σ allowed region is not bounded on the left, allowing a vanishing $\sin^2 2\vartheta_{ee}$ which corresponds to the absence of short-baseline oscillations.

Note that a more reliable estimate of the statistical significance of the indications in favor of neutrino oscillations would require Monte Carlo simulations, because of the violation of Wilks' theorem [29, 51, 58, 59]. However, these simulations are very difficult, because they require detailed knowledge of all the experimental features and huge computing times. Therefore, in this work we discuss only the results obtained assuming the standard χ^2 distribution, as done in the great majority of publications.

In the following we discuss the compatibility of the results of the fits of reactor spectral ratio data with the neutrino oscillation interpretation of the Gallium data and we perform combined fits with other experimental results. For convenience, we introduce the following notation:

RSRF(N/DB): combined reactor spectral ratio fit of the NEOS/Daya Bay, DANSS, PROSPECT,

STEREO, and Bugey-3 data.

RSRF(N/R): combined reactor spectral ratio fit of the NEOS/RENO, DANSS, PROSPECT, STEREO, and Bugey-3 data.

As shown in Fig. 4, these combined fits of the data of reactor spectral ratio experiments favor short-baseline neutrino oscillations at values of Δm_{41}^2 which are compatible with the neutrino oscillation interpretation of the Gallium data discussed in Section II, but the required values of the mixing angle are smaller. Therefore, there is a tension between the results of reactor spectral ratio experiments and those of the Gallium experiments. This tension is quantified by the values of the parameter goodness of fit in Tab. III. For all the four Gallium detection cross section models, the parameter goodness of fit is well below 1% for RSRF(N/DB), whereas it is slightly above 1% for RSRF(N/R). The larger compatibility of RSRF(N/R) with the Gallium data may seem contradictory with the smaller statistical significance of short-baseline neutrino oscillations of RSRF(N/R) (2.6σ) with respect to RSRF(N/DB) (3.1σ). However, one can see from Fig. 4 that the 3σ allowed region of RSRF(N/R) extends to large values of $\sin^2 2\vartheta_{ee}$ for large values of Δm_{41}^2 , leading to a relative compatibility with the Gallium allowed regions. On the other hand, the 3σ allowed regions of RSRF(N/DB) are closed and lie at values of $\sin^2 2\vartheta_{ee}$ that are incompatible with the Gallium allowed regions.

Note that since the data sets considered in this paper are not the same as those of Ref. [29], we obtain quantitatively different results. As noted above, the combined analysis of reactor spectral ratios in Ref. [29] includes the Neutrino-4 data, which shift the best fit value into the region allowed by the analysis of the Gallium data (see Tab. 1 of Ref. [29]). As can be seen in the lower right panel of Fig. 2 of Ref. [29], the 2σ island around the best fit value lies at relatively large mixing and has a sizable overlap with the region preferred by the Gallium analysis, shown in the left panel of Fig. 4 of Ref. [29]. Therefore, the authors of Ref. [29] obtain a large parameter goodness of fit p -value for the combined analysis of the reactor spectral ratio data and Gallium data (see Tab. 5 of Ref. [29]). In our combined reactor spectral ratio analysis, using the newest DANSS data and omitting the Neutrino-4 data leads to regions which are quite small at the 2σ level (even at the 3σ level for RSRF(N/DB)) and far away from the Gallium allowed regions. Therefore, we find a significant tension between the fits of the reactor spectral ratio data and the Gallium data.

V. Combined short-baseline reactor spectral ratios and rates

It is interesting to combine the results of the analyses of the reactor spectral ratio data with the results of

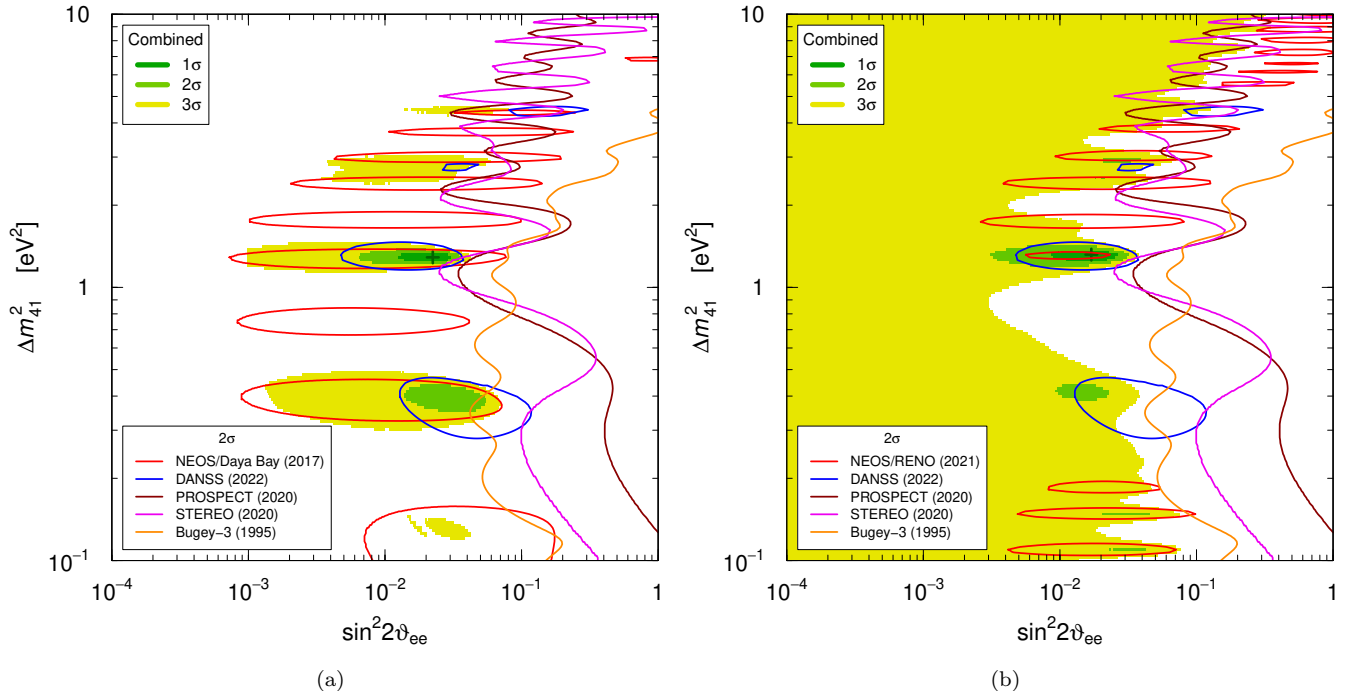


FIG. 3. Allowed regions in the $(\sin^2 2\vartheta_{ee}, \Delta m_{41}^2)$ plane obtained from the combined analysis of the (a) NEOS/Daya Bay [45] or (b) NEOS/RENO [46] spectral ratio data with those of the DANSS [40], PROSPECT [42], STEREO [44], and Bugey-3 [57] experiments. Also shown are the contours of the 2σ allowed regions of each experiments. Closed contours surround the allowed region and open contours exclude the region on the right.

	RSRF(N/DB)		RSRF(N/R)	
	$\Delta\chi_{PG}^2$	GoF _{PG}	$\Delta\chi_{PG}^2$	GoF _{PG}
Ground State	12.95	0.15%	8.91	1.2%
Bahcall	12.86	0.16%	8.74	1.3%
Kostensalo	12.91	0.16%	8.89	1.2%
Semenov	12.88	0.16%	8.70	1.3%

TABLE III. χ^2 difference $\Delta\chi_{PG}^2$ of the parameter goodness of fit test [36] applied to the comparison of the neutrino oscillation fits of the reactor spectral ratio data and the Gallium data with the four Gallium detection cross sections in Tab. I. The values of the corresponding parameter goodness of fit GoF_{PG} are calculated with two degrees of freedom corresponding to the two common oscillation parameters $\sin^2 2\vartheta_{ee}$ and Δm_{41}^2 . The column titles RSRF(N/DB) and RSRF(N/R) indicate, respectively, the combined fits of NEOS/Daya Bay and NEOS/RENO data with those of the other reactor spectral ratio experiments discussed in the text (DANSS, PROSPECT, STEREO, and Bugey-3).

the analyses of the reactor rate data discussed in Section III and to compare the combination with the results of the analyses of the Gallium data discussed in Section II. Fig. 5 shows the comparison of the corresponding 2σ and 3σ allowed regions.

Comparing Fig. 5(a) with Fig. 4, one can see that the addition of the reactor rate data leads to a better localization of the reactor 2σ allowed regions in the RSRF(N/DB) analysis, for all the reactor flux models. In this case there are only two 2σ -allowed islands at $\Delta m_{41}^2 \simeq 1.3 \text{ eV}^2$ and $\Delta m_{41}^2 \simeq 0.4 \text{ eV}^2$ for the HM, EF, and KI reactor flux models. The first 2σ -allowed island surrounds the best-fit point at $\sin^2 2\vartheta_{ee} = 0.022$. With the HKSS reactor flux models there is also a third small 2σ -allowed

island at $\Delta m_{41}^2 \simeq 12 \text{ eV}^2$ and $\sin^2 2\vartheta_{ee} = 0.13 - 0.17$, indicating a larger compatibility with the Gallium data. However, in this case the best-fit point lies in the second 2σ -allowed island at $\sin^2 2\vartheta_{ee} = 0.04$. Figure 5(c) shows the 3σ -allowed regions obtained with the combined analysis of RSRF(N/DB) and reactor rates. One can see that the HM and HKSS reactor flux models give large 3σ -allowed regions at large values of Δm_{41}^2 , which include relatively large values of $\sin^2 2\vartheta_{ee}$ and partially overlap with the Gallium 3σ -allowed regions. Also the EF reactor flux model has some small 3σ -allowed regions at large values of Δm_{41}^2 , but there is only little overlap with the Gallium 3σ -allowed regions and only when considering the extreme Ground State cross section model. The

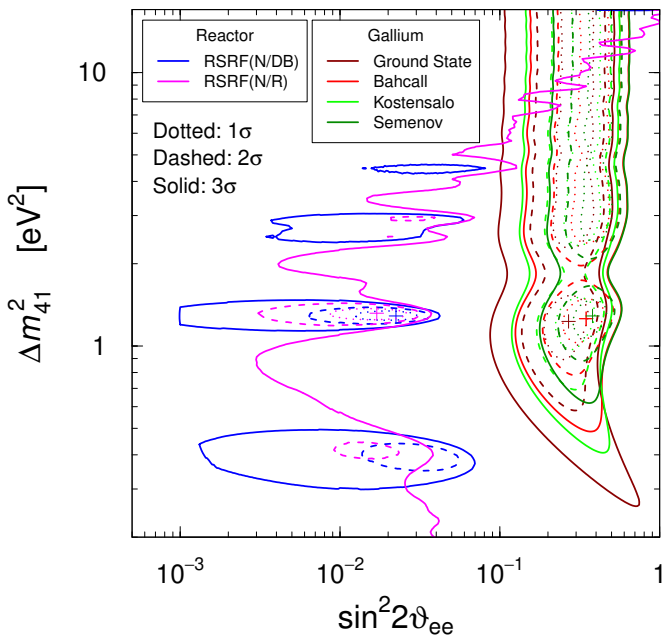


FIG. 4. Contours delimiting the 1σ , 2σ , and 3σ allowed regions in the $(\sin^2 2\vartheta_{ee}, \Delta m_{41}^2)$ plane obtained from the Gallium data with different cross sections compared with those obtained from the two analyses of reactor spectral ratio data discussed in the text. The best-fit points are indicated by crosses.

KI reactor flux model does not yield any 3σ -allowed region at large values of Δm_{41}^2 and is in strongest tension with the Gallium 3σ -allowed region. The tension in the different cases is quantified by the values of the parameter goodness of fit in Tab. IV, where one can see that the fits with all the Gallium cross section models are in very strong and unacceptable tension with the reactor RSRF(N/DB) + KI fit. The tension is smaller, but still very strong and unacceptable in the case of the reactor RSRF(N/DB) + EF fit. The GoF_{PG} is below 0.1% for the RSRF(N/DB) + HM fit and also below 1% for the RSRF(N/DB) + HKSS fit.

Let us now discuss the results of the combined analysis of RSRF(N/R) and the reactor rates, that are shown in Figs. 5(b) and 5(d). Comparing with Figs. 5(a) and 5(c), one can see that the constraints on the mixing parameters are looser than in the combined analysis of RSRF(N/DB) and reactor rates. In particular, from Fig. 5(b) one can see that the combined analyses of RSRF(N/R) and reactor rates with the HM and HKSS reactor flux models yields large 2σ -allowed regions at large values of Δm_{41}^2 and relatively large values of $\sin^2 2\vartheta_{ee}$, with partial overlaps with the Gallium 2σ -allowed regions obtained with the Ground State, Bahcall, and Kostensalo Gallium cross section models. Figure 5(d) shows that the combined analyses of RSRF(N/R) and reactor rates with all the reactor flux models yield only exclusion curves at 3σ , but there are significant overlaps of the allowed regions with some of the Gallium 3σ -allowed regions. There-

fore, as shown in Tab. IV, the tension between reactor and Gallium data is smaller for the combined analyses of RSRF(N/R) and reactor rates than for the combined analyses of RSRF(N/DB) and reactor rates. One can see from Tab. IV that nevertheless the tension is very strong and unacceptable in the case of the reactor RSRF(N/R) + KI fit. The tension is smaller, but still with GoF_{PG} well below 0.1% in the case of the reactor RSRF(N/R) + EF fit. The GoF_{PG} is also below 1% for the RSRF(N/R) + HM fit. Only when considering the RSRF(N/R) + HKSS fit and the Ground State Gallium cross section model we find $\text{GoF}_{\text{PG}} > 1\%$.

VI. The KATRIN limit

The Karlsruhe Tritium Neutrino (KATRIN) experiment provides the current strongest laboratory limit on the absolute mass of light neutrinos. It aims to measure the end point region of the spectrum of molecular tritium β -decay ($T_2 \rightarrow {}^3\text{HeT}^+ + e^- + \bar{\nu}_e$) with high enough precision to discern the shape distortion caused by tiny neutrino masses. The first (second) data taking campaign set an upper bound of 1.1 eV (0.9 eV) at 90% C.L. on the effective electron neutrino mass m_β , which, in the standard three-neutrino mixing framework is defined as

$$m_\beta^2 = \sum_{i=1}^3 |U_{ei}|^2 m_i^2. \quad (2)$$

An upper bound of 0.8 eV at 90% C.L. is obtained when data from both campaigns are combined [60]. Data from KATRIN has already been used to search for light sterile neutrinos, see Refs. [50, 61, 62]. In this work we use the data from the second campaign to constrain Δm_{41}^2 and $\sin^2 2\vartheta_{ee}$. While we follow the general analysis approach of the KATRIN Collaboration, as described in Ref. [62], there are some differences which we discuss below.

The differential spectrum $R_\beta(E)$ of β -decay can be calculated using Fermi's Golden Rule:

$$R_\beta(E, m_\beta^2) = \frac{G_F^2 \cos^2 \theta_C}{2\pi^3} |M_{\text{nuc}}|^2 F(E, Z) \times (E + m_e) \sqrt{(E + m_e)^2 - m_e^2} \times \sum_j P_j \epsilon_j \sqrt{\epsilon_j^2 - m_\beta^2} \Theta(\epsilon_j - m_\beta^2). \quad (3)$$

Here G_F is the Fermi constant, θ_C is the Cabibbo angle, M_{nuc} is the nuclear matrix element, m_e is the electron mass, E is the kinetic energy of the emitted electron, $F(E, Z)$ is the relativistic Fermi function, $\epsilon_j = E_0 - E - V_j$ are the neutrino energies, where E_0 is the end point energy of gaseous molecular tritium (T_2) and V_j are the energies of the various excited final states which occur with probabilities P_j [63]. Measurements of the atomic mass difference of tritium and ${}^3\text{He}$ [64] have found the Q -value to be 18575.72 ± 0.07 eV. This Q -value corresponds to the end point $E_0 = 18574.21 \pm 0.6$ eV [60].

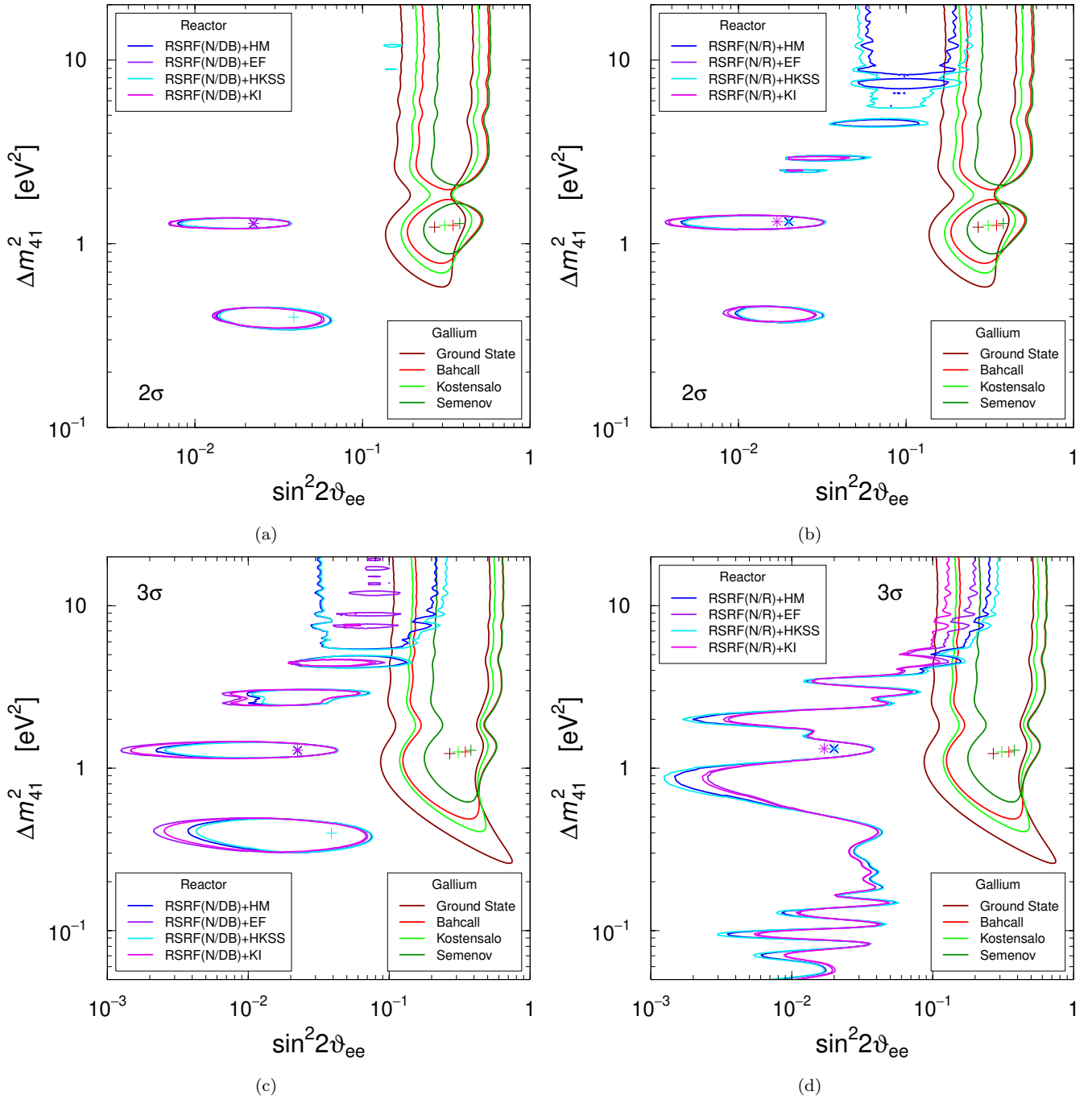


FIG. 5. Comparison of the contours delimiting the [(a) and (b)] 2σ and [(c) and (d)] 3σ allowed regions in the $(\sin^2 2\vartheta_{ee}, \Delta m_{41}^2)$ plane obtained from the combined analysis of the data of the reactor rate experiments with different flux models and the spectral ratio experiments with those obtained from the Gallium data with different cross sections. The figures differ by the use of [(a) and (c)] NEOS/Daya Bay [45] or [(b) and (d)] NEOS/RENO [46] spectral ratio data. The best-fit points are indicated by crosses.

The KATRIN detector measures the integral spectrum

which, at a retarding potential qU_i , is given by

$$R_{\text{model}}(qU_i) = A_{\text{sig}} N_T \int_{qU_i}^{E_0} R_{\beta}(E) f(E - qU_i) dE + R_{\text{bg}}(qU_i). \quad (4)$$

RSRF(N/DB) + Reactor Rates								
	HM		HKSS		EF		KI	
	$\Delta\chi_{\text{PG}}^2$	GoF _{PG}						
Ground State	14.30	0.078%	11.36	0.34%	19.57	0.0056%	21.81	0.0018%
Bahcall	18.33	0.01%	15.16	0.051%	23.60	0.00075%	26.02	0.00022%
Kostensalo	17.04	0.02%	13.80	0.1%	22.30	0.0014%	27.51	0.00011%
Semenov	23.22	0.00091%	19.39	0.0061%	28.28	0.000072%	36.85	0.00000099%
RSRF(N/R) + Reactor Rates								
	HM		HKSS		EF		KI	
	$\Delta\chi_{\text{PG}}^2$	GoF _{PG}						
Ground State	10.12	0.63%	6.94	3.1%	15.59	0.041%	21.04	0.0027%
Bahcall	14.14	0.085%	10.72	0.47%	19.61	0.0055%	25.63	0.00027%
Kostensalo	12.84	0.16%	9.36	0.93%	18.30	0.011%	24.89	0.00039%
Semenov	19.04	0.0073%	15.00	0.055%	24.29	0.00053%	32.99	0.0000068%

TABLE IV. χ^2 difference $\Delta\chi_{\text{PG}}^2$ of the parameter goodness of fit test [36] applied to the comparison of the neutrino oscillation fits of the reactor rates and spectral ratio data with the Gallium data using the four Gallium detection cross sections in Tab. I. The values of the corresponding parameter goodness of fit GoF_{PG} are calculated with two degrees of freedom corresponding to the two common oscillation parameters $\sin^2 2\vartheta_{ee}$ and Δm_{41}^2 . The column titles RSRF(N/DB) and RSRF(N/R) indicate, respectively, the combined fits of NEOS/Daya Bay and NEOS/RENO data with those of the other reactor spectral ratio experiments discussed in the text (DANSS, PROSPECT, STEREO, and Bugey-3). The column titles HM, HKSS, EF, and KI refer to the four reactor neutrino fluxes discussed in Section III.

The differential spectrum $R_\beta(E)$ is convoluted with the experimental response function $f(E - qU_i)$. The response function describes the probability for an electron emitted with kinetic energy E to reach the detector when the retarding potential is qU_i . We use the green dotted line in Fig. 5 of Ref. [60] for the response function. In the above equation, N_T and A_{sig} are the effective number of tritium atoms in the source and the signal amplitude respectively. Since we are interested in performing a shape only analysis, N_T and A_{sig} are combined into a normalization factor N which is left free in the analysis. The background rate $R_{bg}(qU_i)$ has three components

$$R_{bg}(qU_i) = R_{bg}^{\text{base}} + R_{bg}^{qU}(qU_i) + R_{bg}^{\text{Penning}}(t(qU_i)), \quad (5)$$

where $t(qU_i)$ is the time spent at the retarding potential qU_i . The dominant contribution comes from the flat constant rate R_{bg}^{base} . A hypothetical qU -dependent background $R_{bg}^{qU}(qU_i)$, with slope constrained to (0.0 ± 4.74) mcps/keV, and a scan-time dependent background $R_{bg}^{\text{Penning}}(t(qU_i))$, constrained to (3 ± 3) μ cps/s, give smaller contributions. Pull terms are added to the χ^2 function to account for the constraints on the subdominant background rates.

For the case of a sterile neutrino with mass m_4 and active-sterile mixing $|U_{e4}|$, the expected rate is

$$R_{\text{pred}}(E, m_\beta^2, m_4^2, |U_{e4}|^2) = (1 - |U_{e4}|^2) R_\beta(E, m_\beta^2) + |U_{e4}|^2 R_\beta(E, m_4^2). \quad (6)$$

To infer the parameters of interest, we perform fits with

fixed Δm_{41}^2 and $|U_{e4}|^2$ pairs, minimizing the function

$$\chi^2 = [\Delta\vec{R}]^T C^{-1} [\Delta\vec{R}] + \left(\frac{m^{qU}}{4.74}\right)^2 + \left(\frac{m^{\text{Penn}} - 3}{3}\right)^2 + \left(\frac{E_0 - 18574.21}{0.6}\right)^2, \quad (7)$$

where $\Delta\vec{R} = \vec{R}_{\text{obs}}(q\vec{U}) - \vec{R}_{\text{pred}}(q\vec{U}, \vec{\eta})$, m^{qU} and m^{Penn} are the slopes of the background components and C^{-1} is the (inverse) covariance matrix provided by the collaboration. To verify our analysis method we first reproduced the standard three-neutrino results and obtained an upper bound of $m_\beta < 0.83$ eV at 90% C.L. and a best fit $m_\beta^2 = 0.1$ eV². These results validate our analysis and so we proceed with the sterile analysis.

There are six nuisance parameters, the overall normalization N , the end point E_0 , the three background parameters and the effective neutrino mass-squared m_β^2 , which are marginalized over. We performed two analyses. In one we fixed $m_\beta = 0$ (so that $\Delta m_{41}^2 = m_4^2$) and in the other m_β was left free and marginalized over. The contours resulting from these analyzes are shown in Fig. 6. The red exclusion curves correspond to the analysis where we fix $m_\beta = 0$. The results of our analysis are in excellent agreement with the results obtained by the KATRIN collaboration [62] in this case. We find that KATRIN data alone disfavor the preferred region from Gallium experiments for mass splittings $\Delta m_{41}^2 \gtrsim 100$ eV². The global minimum of the χ^2 function is $\chi^2 = 27.59$ at $\Delta m_{41}^2 = 50.6$ eV² and $\sin^2 2\vartheta_{ee} = 0.05$ ($|U_{e4}|^2 = 0.013$). The significance over the null hypothesis is $\Delta\chi^2 = 0.38$. The blue contours in

	RSRF(N/DB) + Reactor Rates + Tritium							
	HM		HKSS		EF		KI	
	$\Delta\chi_{\text{PG}}^2$	GoF _{PG}	$\Delta\chi_{\text{PG}}^2$	GoF _{PG}	$\Delta\chi_{\text{PG}}^2$	GoF _{PG}	$\Delta\chi_{\text{PG}}^2$	GoF _{PG}
Ground State	15.69	0.039%	13.17	0.14%	20.82	0.003%	21.82	0.0018%
Bahcall	19.86	0.0049%	17.19	0.019%	25.06	0.00036%	26.03	0.00022%
Kostensalo	18.63	0.009%	15.87	0.036%	23.83	0.00067%	27.52	0.00011%
Semenov	25.22	0.00033%	21.94	0.0017%	30.42	0.000025%	37.42	0.0000075%
	RSRF(N/R) + Reactor Rates + Tritium							
	HM		HKSS		EF		KI	
	$\Delta\chi_{\text{PG}}^2$	GoF _{PG}	$\Delta\chi_{\text{PG}}^2$	GoF _{PG}	$\Delta\chi_{\text{PG}}^2$	GoF _{PG}	$\Delta\chi_{\text{PG}}^2$	GoF _{PG}
Ground State	11.56	0.31%	8.72	1.3%	16.96	0.021%	21.49	0.0022%
Bahcall	15.76	0.038%	12.74	0.17%	21.19	0.0025%	26.08	0.00022%
Kostensalo	14.49	0.071%	11.40	0.33%	19.97	0.0046%	25.37	0.00031%
Semenov	21.04	0.0027%	17.45	0.016%	26.45	0.00018%	33.56	0.0000052%

TABLE V. χ^2 difference $\Delta\chi_{\text{PG}}^2$ of the parameter goodness of fit test [36] applied to the comparison of the neutrino oscillation fits of the reactor rates, spectral ratio data, and tritium data with the Gallium data using the four Gallium detection cross sections in Tab. I. The values of the corresponding parameter goodness of fit GoF_{PG} are calculated with two degrees of freedom corresponding to the two common oscillation parameters $\sin^2 2\vartheta_{ee}$ and Δm_{41}^2 . The column titles RSRF(N/DB) and RSRF(N/R) indicate, respectively, the combined fits of NEOS/Daya Bay and NEOS/RENO data with those of the other reactor spectral ratio experiments discussed in the text (DANSS, PROSPECT, STEREO, and Bugey-3). The column titles HM, HKSS, EF, and KI refer to the four reactor neutrino fluxes discussed in Section III.

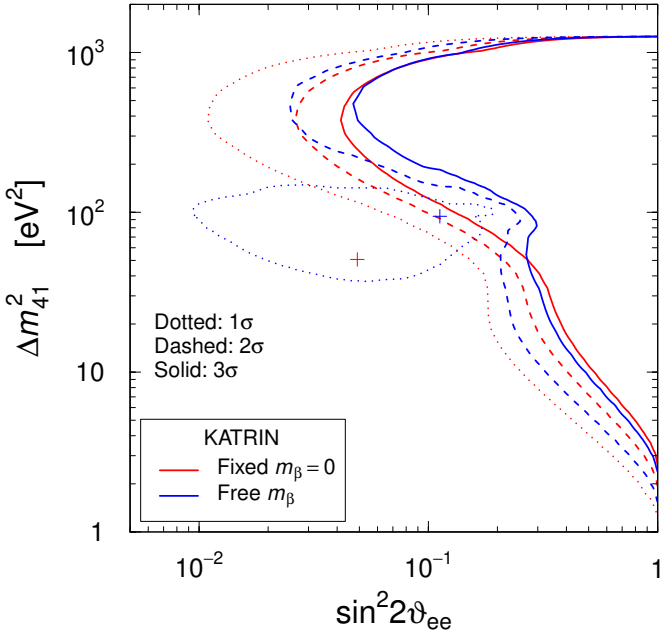


FIG. 6. Contours delimiting the 1σ , 2σ , 3σ allowed regions in the $(\sin^2 2\vartheta_{ee}, \Delta m_{41}^2)$ plane obtained from the analysis of KATRIN run 2 data. Red curves correspond to the analysis with fixed $m_\beta = 0$, while the blue curves are obtained after marginalizing over a free m_β . The best-fit points are indicated by crosses.

Fig. 6 are obtained when marginalizing over the free m_β . In contrast to the collaboration's approach, we require that the neutrino mass is real ($m_\beta^2 \geq 0$) and $m_4 > m_\beta$.

The analysis with free m_β gives minimum $\chi^2 = 25.27$ at $\Delta m_{41}^2 = 87.8 \text{ eV}^2$ ($m_4^2 = 88.7 \text{ eV}^2, m_\beta^2 = 0.9 \text{ eV}^2$) and $\sin^2(\vartheta_{ee}) = 0.11$ ($|U_{e4}|^2 = 0.029$). The preference over the no sterile hypothesis is larger ($\Delta\chi^2 = 2.7$) but still not very significant. This explains the closed 1σ contour in Fig. 6. Such a small preference has already been observed in former analyses [50] of KATRIN data. We consider these results more accurate than the collaboration's result, since we do not allow for any parameters to go into an unphysical region of the parameter space in the marginalization process. The bounds become rapidly weak beyond $\Delta m_{41}^2 \sim 10^3 \text{ eV}^2$ because the decay spectrum is only available up to 40 eV away from the end point.

VII. Combination of short-baseline reactor data and Tritium constraints

Before the on-going KATRIN experiment, there have been many experiments on the search of the effects of neutrino masses in β decays, following the basic idea presented by Enrico Fermi in 1933 in the same article in which he formulated the theory of weak interactions [65]. The strongest limits have been obtained in Tritium β -decay experiments (see, e.g., the recent review in Ref. [66]). Some experiments have measured the electron spectrum in a large energy interval below the end point. Since none of these experiments found a deviation of the electron spectrum from that predicted in the case of massless neutrino, they produced bounds on the mixing of a heavy neutrino with the electron neutrino which

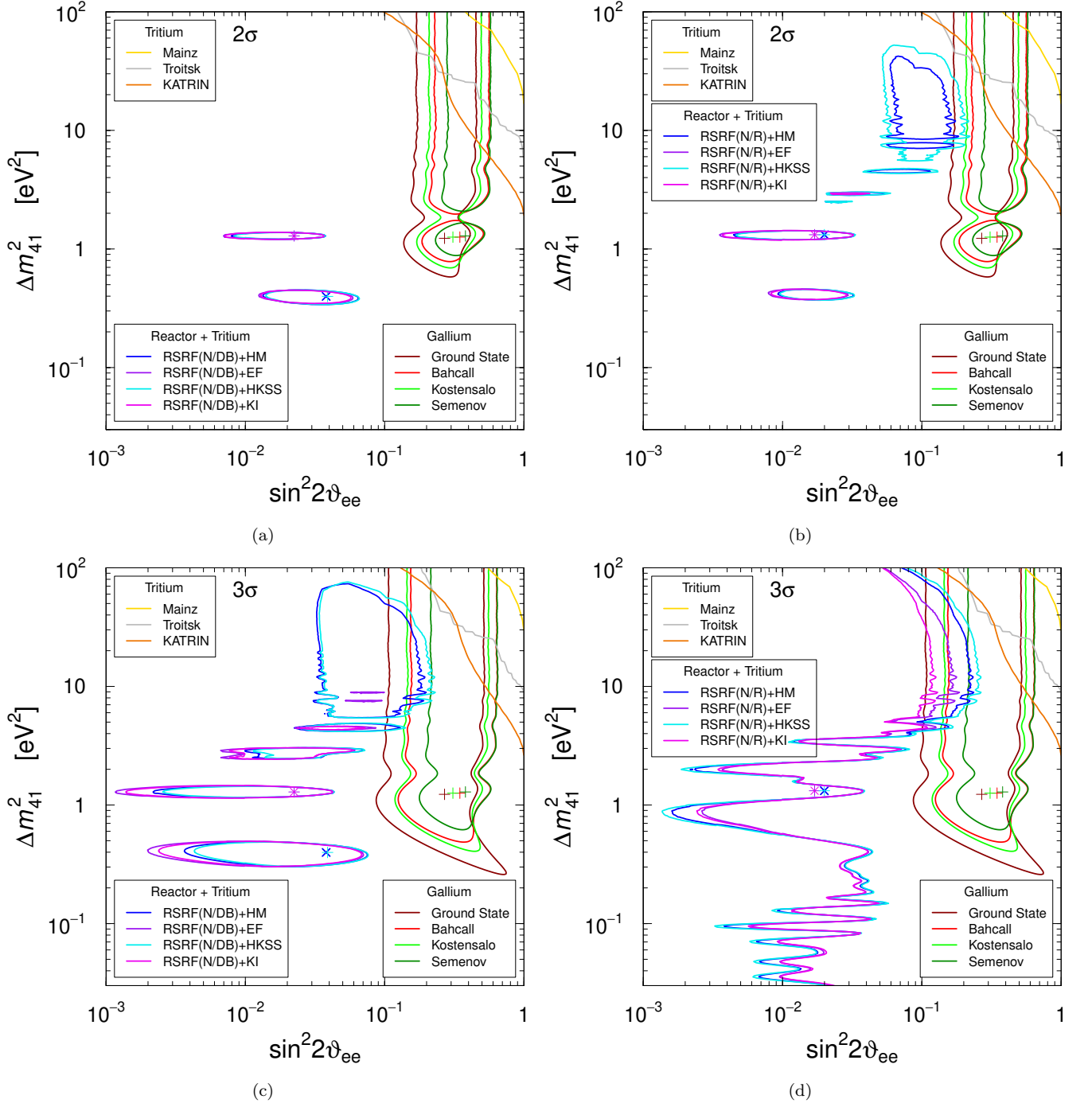


FIG. 7. Comparison of the contours delimiting the [(a) and (b)] 2σ and [(c) and (d)] 3σ allowed regions in the $(\sin^2 2\vartheta_{ee}, \Delta m_{41}^2)$ plane obtained from the combined analysis of the data of the reactor rate experiments with different flux models, the spectral ratio experiments, and the Tritium experiments with those obtained from the Gallium data with different cross sections. The figures differ by the use of [(a) and (c)] NEOS/Daya Bay [45] or [(b) and (d)] NEOS/RENO [46] spectral ratio data. The best-fit points are indicated by crosses.

depend on the mass of the heavy neutrino. In the framework of 3+1 active-sterile neutrino mixing, the results of these experiments imply bounds on $|U_{e4}|^2$ and the corresponding $\sin^2 2\vartheta_{ee} = 4|U_{e4}|^2(1 - |U_{e4}|^2)$ which depend on the value of m_4 .

In this section we present the results of the combined analysis of short-baseline reactor data and the Tritium data. We assume that the three standard neutrino masses m_1 , m_2 , and m_3 are much lighter than m_4 , so that $\Delta m_{41}^2 \simeq m_4^2$.

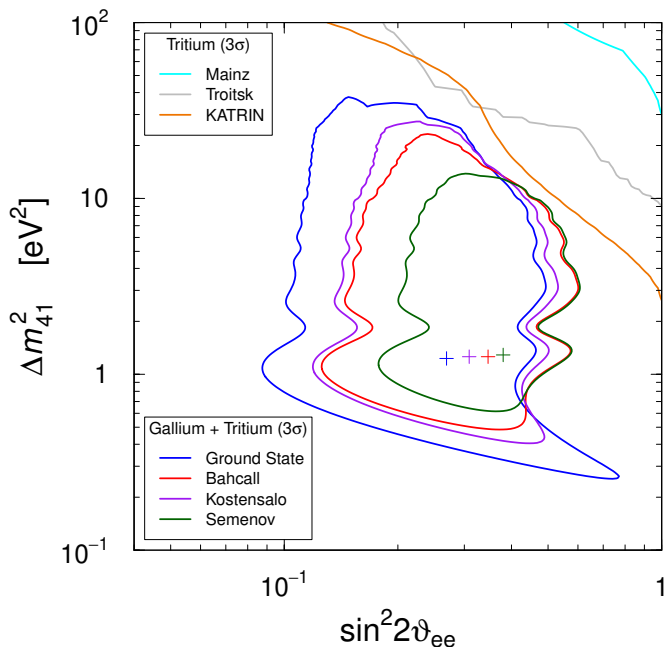


FIG. 8. Contours delimiting the 3σ allowed regions in the $(\sin^2 2\vartheta_{ee}, \Delta m_{41}^2)$ plane obtained from the combined analysis of the Gallium data with different cross sections and the Tritium data. The figure shows also the 3σ exclusion curves of the Mainz, Troitsk, and KATRIN Tritium experiments.

Besides the KATRIN bounds presented in Section VI, we consider the bounds of the previous Tritium experiments Mainz [67] and Troitsk [68, 69]. For these experiments, we use the results obtained in Ref. [70] and already used in several papers (e.g., Refs. [48, 50]). The reason for considering also the Troitsk bound is illustrated in Fig. 7, where one can see that the Troitsk bound is competitive with the KATRIN limit at large values of Δm_{41}^2 and cannot be neglected. For completeness we consider also the less strong Mainz bound, which is shown in Fig. 7, because Mainz and Troitsk have been contemporary and competitive experiments of the generation before KATRIN.

In Fig. 7 we show the combined 2σ and 3σ allowed regions in the $(\sin^2 2\vartheta_{ee}, \Delta m_{41}^2)$ plane obtained from the data of the reactor rate experiments with different flux models, the spectral ratio experiments, and the three Tritium experiments KATRIN, Troitsk and Mainz. Comparing Fig. 7(c) with Fig. 5(c), one can see that when the NEOS/Daya Bay data are used (RSRF(N/DB) fit) the large- Δm_{41}^2 3σ allowed regions in the cases of the HM and HKSS reactor flux models are limited by the bounds of the Tritium experiments. When the NEOS/RENO data are used (RSRF(N/R) fit), all the reactor flux models give 3σ exclusion curves. Comparing Figs. 7(b) and 7(d) with Figs. 5(b) and 5(d), one can see that the Tritium data allow us to improve the exclusion of large mixing for large values of Δm_{41}^2 .

The addition of the Tritium bounds increases the tension between the reactor data and the Gallium data in

the framework of short-baseline active-sterile oscillations. This can be seen by comparing the values of the parameter goodness of fit in Tabs. IV and V.

For completeness, in Fig. 8 we show the regions in the $(\sin^2 2\vartheta_{ee}, \Delta m_{41}^2)$ plane which are allowed at 3σ by the combined analysis of the Gallium data with different cross sections and the data of the Mainz, Troitsk, and KATRIN Tritium experiments. Comparing the combined allowed regions with those in Fig. 7, one can see that the Tritium bounds reduce the Gallium allowed regions at large values of Δm_{41}^2 , limiting the 3σ allowed regions at $\Delta m_{41}^2 \lesssim 30 \text{ eV}^2$. This figure is useful for discussions of the Gallium Anomaly in which the bounds from other experiments (i.e. those of the reactor experiments discussed above and the solar neutrino bound discussed in Section VIII) are not considered.

VIII. The solar neutrino bound

Solar neutrinos provide a robust method to constrain ν_e disappearance at short baselines [73–78]. The solar neutrino data include the measurements from three distinct channels, i.e., charged current (CC) interactions [25, 28, 79, 80], neutral current (NC) interactions [80], and electron-scattering (ES) interactions [80–86]. Each of the detection channels is sensitive to a different combination of the electron neutrino ν_e , and the other active neutrinos ν_μ, ν_τ . In the framework of the 3+1 neutrino mixing scheme, both the electron neutrino survival probability P_{ee} and the electron-to-sterile neutrino transitional probability P_{es} can be constrained with these CC, NC and ES measurements. In this work, we employ the simplified treatment of the solar neutrino analysis proposed in Ref. [77], where only the asymptotic values of P_{ee} and P_{es} at the high and low energies are employed to constrain the relevant mixing parameters. This method has been proven to consistently reproduce the full data analysis treatment [77], since the eV-scale sterile neutrinos do not modify the energy dependence of the MSW resonance region in the oscillation probabilities [73].

In the 3+1 mixing scheme, the solar neutrino oscillation probabilities P_{ee} and P_{es} can be written as

$$P_{ee} = \sum_{k=1}^4 |U_{ek}^m|^2 |U_{ek}|^2, \quad P_{es} = \sum_{k=1}^4 |U_{ek}^m|^2 |U_{sk}|^2, \quad (8)$$

where U_{ek}^m is the mixing element in matter at the production point of solar neutrinos. By using the parametrization of the mixing matrix U in Ref. [73], the low energy (LE) and high energy (HE) asymptotic values of P_{ee} and P_{es} can be easily calculated as

$$P_{ee}^{\text{LE}} = c_{12}^4 c_{13}^4 c_{14}^4 + s_{12}^4 s_{13}^4 c_{14}^4 + s_{13}^4 c_{14}^4 + s_{14}^4, \quad (9)$$

$$P_{ee}^{\text{HE}} = s_{12}^2 c_{13}^4 c_{14}^4 + s_{13}^4 c_{14}^4 + s_{14}^4, \quad (10)$$

$$P_{es}^{\text{LE}} = (c_{12}^4 c_{13}^4 + s_{12}^4 c_{13}^4 + s_{13}^4 + 1) s_{14}^2 c_{14}^2, \quad (11)$$

$$P_{es}^{\text{HE}} = (s_{12}^2 c_{13}^4 + s_{13}^4 + 1) s_{14}^2 c_{14}^2, \quad (12)$$

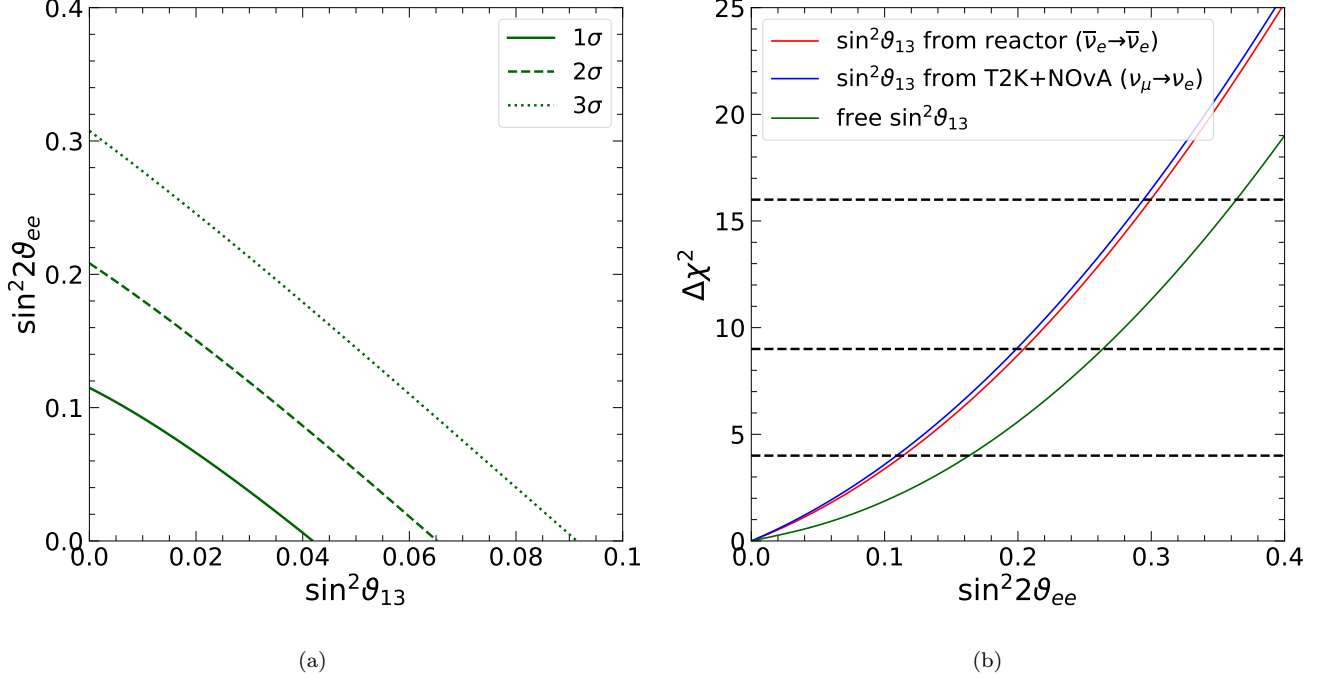


FIG. 9. (a) Allowed region in the $(\sin^2 \vartheta_{13}, \sin^2 2\vartheta_{ee})$ plane from the global solar data with free $\sin^2 \vartheta_{12}$. (b) The one-dimensional $\Delta\chi^2$ profiles of $\sin^2 2\vartheta_{ee}$, where the red line corresponds to the analysis including the $\sin^2 \vartheta_{13}$ constraint from PDG 2020 [71], the blue line is for the case of $\sin^2 \vartheta_{13}$ constrained by neutrino data from T2K and NOvA [72], and the green line corresponds to the case with unconstrained $\sin^2 \vartheta_{13}$.

	Solar-only		S+ ϑ_{13} (T&N)		S+ ϑ_{13} (R)	
	$\Delta\chi_{\text{PG}}^2$	GoF _{PG}	$\Delta\chi_{\text{PG}}^2$	GoF _{PG}	$\Delta\chi_{\text{PG}}^2$	GoF _{PG}
Ground State	7.31	2.6%	10.65	0.49%	10.32	0.57%
Bahcall	10.30	0.58%	14.14	0.085%	13.78	0.1%
Kostensalo	9.03	1.1%	12.79	0.17%	12.43	0.2%
Semenov	12.70	0.17%	17.24	0.018%	16.83	0.022%

TABLE VI. χ^2 difference $\Delta\chi_{\text{PG}}^2$ of the parameter goodness of fit test [36] applied to the comparison of the solar neutrino bounds and the neutrino oscillation explanation of the Gallium data with the four Gallium detection cross sections in Tab. I. The values of the corresponding parameter goodness of fit GoF_{PG} are calculated with two degrees of freedom corresponding to the two common oscillation parameters $\sin^2 2\vartheta_{ee}$ and Δm_{21}^2 . The Solar-only, S+ ϑ_{13} (T&N), and S+ ϑ_{13} (R) column titles refer, respectively, to the free $\sin^2 \vartheta_{13}$ analysis, the analysis with $\sin^2 \vartheta_{13}$ constrained by neutrino data from T2K and NOvA, and the analysis with $\sin^2 \vartheta_{13}$ constrained by reactor data.

where $s_{ij} \equiv \sin \vartheta_{ij}$ and $c_{ij} \equiv \cos \vartheta_{ij}$ ($1 \leq i, j \leq 4$) have been used, and $\vartheta_{12}^m(\text{LE}) = \vartheta_{12}$ and $\vartheta_{12}^m(\text{HE}) = \pi/2$ are employed. Before doing the numerical analysis, we make the following comments on the analysis method:

A: $\vartheta_{24} = 0$ and $\vartheta_{34} = 0$ are used in the above calculations, which have been proven to have no visible effects [75–78] on the solar neutrino data when considering the corresponding constraints of ϑ_{24} and ϑ_{34} from measurements of accelerator ν_μ disappearance [87, 88], atmospheric neutrinos [89, 90] and long-baseline accelerator NC interactions [91, 92].

B: KamLAND data [93] is not included in the analysis. But the value of Δm_{21}^2 has been implicitly as-

sumed to not significantly deviate from the current allowed region of the large mixing angle solution of the MSW resonance, and thus does not alter the asymptotic values of oscillation probabilities. This assumption is seen to be valid by considering the allowed range of Δm_{21}^2 from the solar-only analysis [10–12, 94].

The χ^2 function employed in this analysis is

$$\chi^2(s_{12}^2, s_{13}^2, \sin^2 2\vartheta_{ee}) = \sum_{a,b} (O_a - P_a) V_{ab}^{-1} (O_b - P_b), \quad (13)$$

where $P_a = (P_{ee}^{\text{LE}}, P_{ee}^{\text{HE}}, P_{e\mu}^{\text{LE}} + P_{e\tau}^{\text{LE}}, P_{e\mu}^{\text{HE}} + P_{e\tau}^{\text{HE}})$, O_a

are the measurements of the asymptotic values of oscillation probabilities from the full solar neutrino analysis, and V_{ab} is the covariance matrix taking into account possible correlations [77]. The transition probability $P_{e\mu} + P_{e\tau}$ is given by $1 - P_{ee} - P_{es}$. In the following, the notation of $\sin^2 2\vartheta_{ee} \equiv 4s_{14}^2(1 - s_{14}^2)$ will be used for consistency with previous sections.

Figure 9(a) illustrates the allowed regions in the $(\sin^2 \vartheta_{13}, \sin^2 2\vartheta_{ee})$ plane obtained from the analysis of solar neutrino data where $\sin^2 \vartheta_{12}$ has been marginalized over. The green solid, dashed and dotted lines show the allowed regions at 1σ , 2σ and 3σ confidence levels, respectively. One can see that $\sin^2 2\vartheta_{ee}$ and $\sin^2 \vartheta_{13}$ are essentially degenerate as already revealed in Eqs. (9-12). The allowed region is located in the lower-left corner of Fig. 9(a), which indicates that $\sin^2 2\vartheta_{ee} \gtrsim 0.2$ is practically ruled out at the 2σ confidence level, independently of the value of $\sin^2 \vartheta_{13}$. The bound on $\sin^2 2\vartheta_{ee}$ becomes more stringent as $\sin^2 \vartheta_{13}$ increases.

In Fig. 9(b) the one-dimensional χ^2 profiles of $\sin^2 2\vartheta_{ee}$ obtained from solar neutrino data are illustrated. The green line is obtained using only solar neutrino data, in which no external information on ϑ_{13} has been imposed. As can be seen, this bound is already in tension with the preferred region of the Gallium experiments discussed in Section II. In the first column of Tab. VI we report the parameter goodness of fit taking into account only solar neutrino data. As can be seen the GoF_{PG} is below 1% for the Bahcall and Semenov cross section models. Using the Kostensalo cross section model, we find $\text{GoF}_{\text{PG}} \sim 1\%$. Only the extreme case of the Ground State cross section gives $\text{GoF}_{\text{PG}} > 1\%$.

The red line in Fig. 9(b) represents the result when taking into account the reactor antineutrino constraint on $\sin \vartheta_{13}$ from PDG 2020 [71], i.e. $\sin^2 \vartheta_{13} = (2.20 \pm 0.07) \times 10^{-2}$. We find that values $\sin^2 2\vartheta_{ee} > 0.1$ are excluded at 2σ and therefore the tension with Gallium data is further increased. As shown in the right column of Tab. VI, the tension becomes unacceptable for all of the cross section models.

The tension between reactor antineutrino data and Gallium neutrino data was already discussed in Ref. [37]. Therein the authors proposed a CPT-violating solution, where the parameters characterizing neutrino oscillations could differ from their antineutrino counterparts [95]. We show that using the newest solar neutrino data, this solution is not viable anymore. The blue line in Fig. 9(b) shows the result of our solar neutrino analysis by considering the bound on ϑ_{13} obtained from the analysis of the neutrino mode data collected in T2K and NOvA [72], i.e., $\sin^2 \vartheta_{13} = (2.60_{-0.48}^{+1.03}) \times 10^{-2}$. One can see that the bound is even slightly stronger than the former one. This is due to the fact that T2K+NOvA in neutrino mode measure a best fit value which is slightly larger than the reactor antineutrino measurement and, as can be seen from Fig. 9(a), larger values of $\sin^2 \vartheta_{13}$ require smaller values of $\sin^2 2\vartheta_{ee}$. As a result the tension with Gallium data is basically the same as in the case where the reac-

	Global RSRF(N/DB) Fit			
	HM	HKSS	EF	KI
χ_{\min}^2	393.5	395.2	391.2	391.4
GoF	43%	40%	46%	46%
$(\sin^2 2\vartheta_{ee})_{\text{b.f.}}$	0.022	0.022	0.022	0.022
$(\Delta m_{41}^2)_{\text{b.f.}}/\text{eV}^2$	1.29	1.29	1.29	1.29
$\Delta\chi_{4\nu-3\nu}^2$	13.8	14.1	12.6	12.9
$n\sigma_{4\nu-3\nu}$	3.3	3.3	3.1	3.2
	Global RSRF(N/R) Fit			
	HM	HKSS	EF	KI
χ_{\min}^2	386.5	388.3	384.0	384.2
GoF	53%	50%	56%	56%
$(\sin^2 2\vartheta_{ee})_{\text{b.f.}}$	0.017	0.019	0.017	0.017
$(\Delta m_{41}^2)_{\text{b.f.}}/\text{eV}^2$	1.32	1.32	1.32	1.32
$\Delta\chi_{4\nu-3\nu}^2$	10.1	10.3	9.1	9.3
$n\sigma_{4\nu-3\nu}$	2.7	2.8	2.6	2.6

TABLE VII. Results of the global ν_e and $\bar{\nu}_e$ disappearance fits obtained using NEOS/Daya Bay (RSRF(N/DB)) or NEOS/RENO (RSRF(N/R)) data. The column titles HM, HKSS, EF, and KI refer to the four reactor neutrino fluxes discussed in Section III. The table show the minimum value χ_{\min}^2 of χ^2 , the goodness of fit (GoF) with 390 degrees of freedom (the number of data points minus two, corresponding to the two fitted mixing parameters), the best-fit values of $\sin^2 2\vartheta_{ee}$ and Δm_{41}^2 , the χ^2 difference $\Delta\chi_{4\nu-3\nu}^2$ between the 3+1 4ν fit and the 3ν fit, and the statistical significance ($n\sigma_{4\nu-3\nu}$) of the corresponding indication in favor of 3+1 4ν mixing.

tor constraint on ϑ_{13} is used, which can also be seen by comparing the central and right columns of Tab. VI. As a consequence, the CPT-violating solution [37] is ruled out by current solar data in combination with the constraint on ϑ_{13} from the neutrino data of T2K and NOvA [72].

IX. Global ν_e and $\bar{\nu}_e$ disappearance analysis

In this Section we present the results of the global analysis of the ν_e and $\bar{\nu}_e$ disappearance data in the framework of 3+1 active-sterile neutrino mixing. The data that we consider are the reactor rates discussed in Section III, the reactor spectral ratio data discussed in Section IV, the Tritium limits discussed in Sections VI and VII, and the solar neutrino bound discussed in Section VIII. We will discuss the global tension between the data that we consider and the Gallium data if the Gallium Anomaly is considered as due to 3+1 active-sterile neutrino mixing. Since the tension is very strong, we cannot include the Gallium data in a global fit in the framework of 3+1 active-sterile neutrino mixing, and we presume that the Gallium Anomaly is due to other reasons.

The results of the global fits that we obtained with different data sets (NEOS/Daya Bay or NEOS/RENO) and different reactor flux models are listed in Tab. VII.

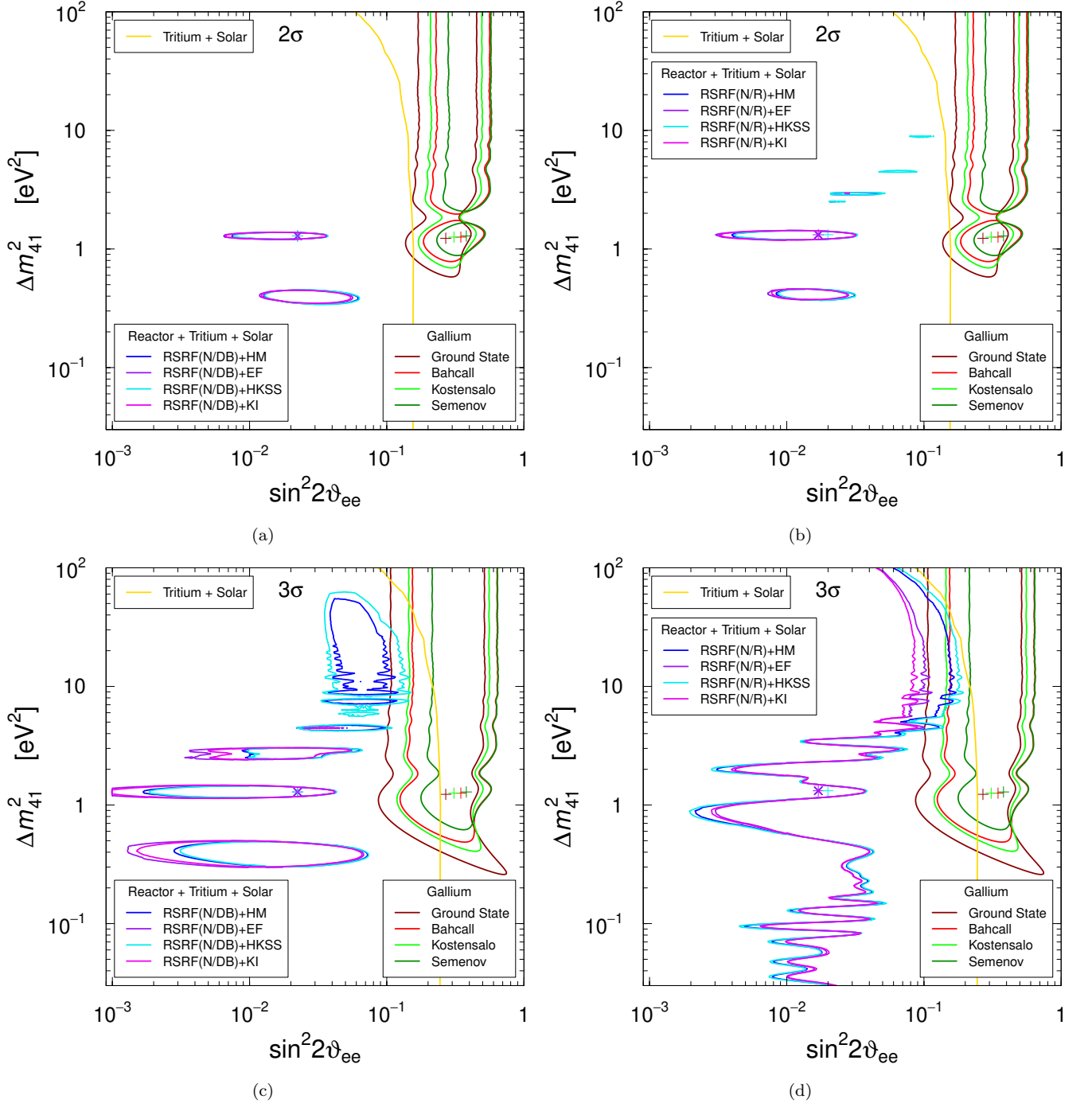


FIG. 10. Comparison of the contours delimiting the [(a) and (b)] 2σ and [(c) and (d)] 3σ allowed regions in the $(\sin^2 2\vartheta_{ee}, \Delta m_{41}^2)$ plane obtained from the combined analysis of the data of the reactor rate experiments with different flux models, the spectral ratio experiments, reactor the Tritium experiments, and the solar bound with those obtained from the Gallium data with different cross sections. Also shown is the 3σ bound obtained from the combination of the Tritium and solar bounds. The figures differ by the use of [(a) and (c)] NEOS/Daya Bay [45] or [(b) and (d)] NEOS/RENO [46] spectral ratio data. The best-fit points are indicated by crosses.

One can see that the goodness of fit is high. There is a $3.1\text{--}3.3\sigma$ indication in favor of $3+1$ active-sterile neutrino mixing in the global fits with the NEOS/Daya Bay data. The indication decreases to $2.6\text{--}2.8\sigma$ if the NEOS/RENO

are used. The values of the best-fit points are in any case around $\sin^2 2\vartheta_{ee} \simeq 0.02$ and $\Delta m_{41}^2 \simeq 1.3 \text{ eV}^2$.

Figure 10 shows the 2σ and 3σ allowed regions in the $(\sin^2 2\vartheta_{ee}, \Delta m_{41}^2)$ plane obtained from the global fits

with different neutrino flux models and considering either the NEOS/Daya Bay [45] spectral ratio (Figs. 10(a) and 10(c)) or the NEOS/RENO [46] spectral ratio (Figs. 10(b) and 10(d)). Comparing Fig. 10 with Fig. 7, one can see that the addition of the solar bound has the effect of reducing the allowed regions for $\sin^2 2\vartheta_{ee} \gtrsim 0.1$. In the case of the fit with the NEOS/Daya Bay spectral ratio, comparing Figs. 10(a) and 10(c) with Figs. 7(a) and 7(c), one can see that the solar bound has the effect of moving the best-fit points obtained with the HM and HKSS reactor neutrino fluxes from the allowed island at $\Delta m_{41}^2 \simeq 0.4 \text{ eV}^2$ to the allowed island at $\Delta m_{41}^2 \simeq 1.3 \text{ eV}^2$, leading to an approximate coincidence of the best-fit points obtained with all the four reactor neutrino fluxes. From Figs. 10(b) and 10(d) one can see that in the analysis with the NEOS/RENO spectral ratio there is a similar approximate coincidence of the best-fit points obtained with all the four reactor neutrino fluxes.

The restrictions of the solar neutrino constraint increase the tension with the results of the Gallium experiments in the framework of 3+1 active-sterile neutrino mixing, as one can see comparing the parameter goodness of fit in Tab. VIII with those in Tab. V, which were obtained without the solar bound. From Tab. VIII, one can see that the global fit gives values of parameter goodness of fit that are well below 1% for all the fits with different data combinations. The values of the parameter goodness of fit in Tab. VIII quantify the tension between the 3σ Gallium allowed regions and the 3σ global allowed regions, which have only marginal overlaps in Fig. 10.

In Fig. 10 one can notice the curious approximate coincidence of the values of Δm_{41}^2 for the global best-fit points ($(\Delta m_{41}^2)_{\text{b.f.}} = 1.3 \text{ eV}^2$) and the Gallium best-fit points ($(\Delta m_{41}^2)_{\text{b.f.}} = 1.3 \text{ eV}^2$ for Bahcall, Kostensalo and Semenov, and $(\Delta m_{41}^2)_{\text{b.f.}} = 1.2 \text{ eV}^2$ for Ground State). This coincidence has no meaning in the framework of 3+1 active-sterile neutrino mixing, because the best-fit values of the unique mixing parameter $\sin^2 2\vartheta_{ee}$ are too different and the 3σ allowed regions are well separated for $\Delta m_{41}^2 \approx 1.3 \text{ eV}^2$.

X. Summary and conclusions

In this paper we discussed in a systematic way the results of ν_e and $\bar{\nu}_e$ disappearance experiments which are relevant for the hypothetical existence of short-baseline neutrino oscillations due to 3+1 active-sterile neutrino mixing. We started in Section II with the analysis of the results of the Gallium source experiments, motivated by the recent results of the BEST experiment [7, 8], which revived the Gallium Anomaly confirming the results of the GALLEX [23–25] and SAGE [20, 26–28] experiments. We have shown that the explanation of the Gallium Anomaly in the framework of 3+1 active-sterile neutrino mixing requires rather large values of the mixing between ν_e and the new massive neutrino ν_4 for all the cross section models of neutrino detection in the Gallium

source experiments. This means that ν_4 is not almost entirely sterile, as it would be required for considering 3+1 active-sterile mixing as a perturbation of standard three-neutrino mixing. This is required for the explanation of the neutrino oscillations observed in solar, atmospheric and long-baseline neutrino oscillation experiments. In Section VIII, we have shown that the neutrino oscillation explanation of the Gallium Anomaly is in strong tension with the solar bound on active-sterile neutrino mixing.

We also considered the results of reactor neutrino experiments and we presented the results of 3+1 fits of the measured rates and the ratios of spectra measured at different distances. In Section III, we have shown that the measured reactor rates imply upper bounds for active-sterile mixing that are in tension with the results of the Gallium experiments for all the cross section models of neutrino detection in the Gallium source experiments and all the reactor neutrino flux models.

In Section IV, we presented the results of a global fit of the most recent available data of the reactor neutrino experiments which measured the ratio of the neutrino spectra at different distances in order to probe neutrino oscillations independently from the absolute values of the neutrino fluxes. Our analysis updates the one of Ref. [29] by taking into account the newest DANSS data which have important effects on the combined analysis of spectral ratio data, as discussed in Section IV. We have shown that the results depend significantly on the choice to consider either the NEOS/Daya Bay [45] or NEOS/RENO [46] spectral ratio data. In the case of the NEOS/Daya Bay, there is a 3.1σ indication in favor of short-baseline oscillations with best-fit parameter values $\sin^2 2\vartheta_{ee} = 0.022$ and $\Delta m_{41}^2 = 1.29 \text{ eV}^2$, which is driven by the overlap of the surrounding allowed regions of NEOS/Daya Bay and DANSS [40]. On the other hand, the overlap of the NEOS/RENO and DANSS allowed regions is smaller and leads to an indication in favor of short-baseline oscillations of only 2.6σ with best-fit parameter values $\sin^2 2\vartheta_{ee} = 0.017$ and $\Delta m_{41}^2 = 1.32 \text{ eV}^2$. Although the NEOS/RENO comparison may be favored by the smaller systematic uncertainties which were estimated by the NEOS and RENO collaborations using the fact that the two experiments detect neutrino fluxes from similar reactors in the same complex, we think that we cannot dismiss the NEOS/Daya Bay data, which should be considered as a different measurement based on the Daya Bay neutrino flux measurement. Since we cannot combine the two measurements because the NEOS data would be double counted, we remain with the ambiguity of the two different results which hopefully will be solved by future measurements.

We have also shown that the results of the reactor spectral ratio experiments are in tension with the neutrino oscillation explanation of the Gallium Anomaly and the tension is stronger when the NEOS/Daya Bay data are considered, with about 0.15% parameter goodness of fit for all the Gallium detection cross section models, whereas considering the NEOS/RENO data we obtain

Global Fit: RSRF(N/DB) + Reactor Rates + Tritium + Solar								
	HM		HKSS		EF		KI	
	$\Delta\chi_{\text{PG}}^2$	GoF _{PG}						
Ground State	21.54	0.0021%	19.51	0.0058%	21.92	0.0017%	21.90	0.0018%
Bahcall	25.99	0.00023%	23.88	0.00065%	26.13	0.00021%	26.11	0.00021%
Kostensalo	25.05	0.00036%	22.77	0.0011%	27.62	0.0001%	27.60	0.0001%
Semenov	32.52	0.0000087%	29.93	0.000032%	37.69	0.00000065%	38.81	0.00000037%
Global Fit: RSRF(N/R) + Reactor Rates + Tritium + Solar								
	HM		HKSS		EF		KI	
	$\Delta\chi_{\text{PG}}^2$	GoF _{PG}						
Ground State	17.61	0.015%	15.53	0.042%	22.56	0.0013%	22.66	0.0012%
Bahcall	22.07	0.0016%	19.90	0.0048%	26.82	0.00015%	26.80	0.00015%
Kostensalo	21.11	0.0026%	18.77	0.0084%	26.27	0.0002%	28.45	0.000066%
Semenov	28.57	0.000062%	25.93	0.00023%	34.00	0.0000041%	38.24	0.0000005%

TABLE VIII. χ^2 difference $\Delta\chi_{\text{PG}}^2$ of the parameter goodness of fit test [36] applied to the comparison of the neutrino oscillation fits of the reactor rates, spectral ratio data, tritium data, and solar bound with the Gallium data using the four Gallium detection cross sections in Tab. I. The values of the corresponding parameter goodness of fit GoF_{PG} are calculated with two degrees of freedom corresponding to the two common oscillation parameters $\sin^2 2\vartheta_{ee}$ and Δm_{41}^2 . The column titles RSRF(N/DB) and RSRF(N/R) indicate, respectively, the combined fits of NEOS/Daya Bay and NEOS/RENO data with those of the other reactor spectral ratio experiments discussed in the text (DANSS, PROSPECT, STEREO, and Bugey-3). The column titles HM, HKSS, EF, and KI refer to the four reactor neutrino fluxes discussed in Section III.

about 1.3%. The tensions increase significantly when we consider the combined analysis of reactor spectral ratios and rates discussed in Section V. In particular, considering the recent reactor flux models of Estienne, Fallot *et al* [34] (EF) and of Kopeikin *et al.* [35] (KI), the parameter goodness of fit is about 0.04% or much lower, depending on the consideration of the NEOS/Daya Bay or NEOS/RENO data and a specific Gallium detection cross section model. The minimal tension is obtained with the extreme Ground State Gallium detection cross section model, with the parameter goodness of fit between about 0.002% and 0.04%, and the maximal tension is obtained with the Semenov model [15] with parameter goodness of fits between about $10^{-6}\%$ and $5 \times 10^{-4}\%$.

In Section VI, we presented the results of the analysis of the recent KATRIN data [60, 62] on the measurement of neutrino masses through their effects on the β -decay spectrum of Tritium. We derived limits on 3+1 active-sterile neutrino mixing which we consider more reliable than those presented in Ref. [62] by the KATRIN collaboration, because we did not consider unphysical negative mass-squared values. We have shown that the KATRIN data exclude large values of Δm_{41}^2 , between about a few eV^2 and 10^3eV^2 , for large mixing. Moreover, in Section VII we presented the results of a combined analysis of the reactor data and the data of the Tritium experiments, considering not only the KATRIN experiment, but also the previous Mainz [67] and Troitsk [68, 69], which are relevant. We have shown that with this set of data, the tension with the neutrino oscillation explanation of the Gallium Anomaly is increased with respect to that obtained with the reactor data alone.

We presented in Section VIII the updated solar neutrino bound on the mixing of ν_4 with ν_e , which is in good agreement with the bound from Ref. [77]. Finally, we discuss in Section IX the results of the global fit of the ν_e and $\bar{\nu}_e$ disappearance data. We have quantified the tension of the solar neutrino bound with the neutrino oscillation explanation of the Gallium Anomaly and we have shown that the tension is dramatic in the case of the global fit, with values of the parameter goodness of fit well below 1% for all the cases with different data choices (NEOS/Daya Bay or NEOS/RENO), different reactor flux models, and different Gallium detection cross sections.

In conclusion, we think that the results presented in this paper show the present status of our knowledge on short-baseline ν_e and $\bar{\nu}_e$ disappearance in the framework of 3+1 active-sterile neutrino mixing and the dramatic tension between the neutrino oscillation explanation of the Gallium Anomaly and the results of the other experiments. We conclude that it is very likely that the Gallium Anomaly is not due to neutrino oscillations and some other explanation must be found.

Acknowledgments

We would like to thank: Mikhail Danilov and Nataliya A. Skrobova for sending us the DANSS χ^2 table; Kim Yeongduk, Soo-Bong Kim, Jonghee Yoo, Yoomin Oh, and all the NEOS and RENO collaborations for providing helpful information on the NEOS+RENO data analysis; Thierry Lasserre and Lisa Schlüter for providing

useful information on the KATRIN data, and Sanshiro Enomoto, Leonard Köllenberger, and Alexey Likhov for useful discussions on the KATRIN data analysis at the NuMass 2022 workshop. C.G. and C.A.T. are supported by the research grant “The Dark Universe: A Synergic Multimessenger Approach” number 2017X7X85K under the program “PRIN 2017” funded by the Italian Ministero dell’Istruzione, Università e della Ricerca (MIUR). C.A.T. also acknowledges support from *Departments of Excellence* grant awarded by MIUR and the

research grant *TAsP (Theoretical Astroparticle Physics)* funded by Istituto Nazionale di Fisica Nucleare (INFN). The work of Y.F.Li and Z.Xin was supported by National Natural Science Foundation of China under Grant Nos. 12075255 and 11835013, by the Key Research Program of the Chinese Academy of Sciences under Grant No. XDPB15. O.T. is supported by a grant funded by Italian Ministero degli Affari Esteri e della Cooperazione Internazionale (MAECI) and also by the Indian Prime Minister’s Research Fellow (PMRF) program.

-
- [1] S. Gariazzo, C. Giunti, M. Laveder, Y. F. Li, and E. Zavanin, *J. Phys.* **G43**, 033001 (2016), arXiv:1507.08204 [hep-ph].
- [2] M. Gonzalez-Garcia, M. Maltoni, and T. Schwetz, *Nucl. Phys.* **B908**, 199 (2016), arXiv:1512.06856 [hep-ph].
- [3] C. Giunti and T. Lasserre, *Ann. Rev. Nucl. Part. Sci.* **69**, 163 (2019), arXiv:1901.08330 [hep-ph].
- [4] A. Diaz, C. Argüelles, G. Collin, J. Conrad, and M. Shaevitz, *Phys.Rept.* **884**, 1 (2020), arXiv:1906.00045 [hep-ex].
- [5] S. Boser, C. Buck, C. Giunti, J. Lesgourgues, L. Ludhova, S. Mertens, A. Schukraft, and M. Wurm, *Prog.Part.Nucl.Phys.* **111**, 103736 (2020), arXiv:1906.01739 [hep-ex].
- [6] B. Dasgupta and J. Kopp, *Phys.Rept.* **928**, 63 (2021), arXiv:2106.05913 [hep-ph].
- [7] V. Barinov et al. (BEST), *Phys.Rev.Lett.* **128**, 232501 (2022), arXiv:2109.11482 [nucl-ex].
- [8] V. V. Barinov et al., (2022), 10.1103/Phys-RevC.105.065502, arXiv:2201.07364 [nucl-ex].
- [9] R. L. Workman (Particle Data Group), *PTEP* **2022**, 083C01 (2022).
- [10] P. F. de Salas, D. V. Forero, S. Gariazzo, P. Martinez-Mirave, O. Mena, C. A. Ternes, M. Tortola, and J. W. F. Valle, *JHEP* **2021**, 071 (2020), arXiv:2006.11237 [hep-ph].
- [11] I. Esteban, M. C. Gonzalez-Garcia, M. Maltoni, T. Schwetz, and A. Zhou, *JHEP* **09**, 178 (2020), arXiv:2007.14792 [hep-ph].
- [12] F. Capozzi, E. Di Valentino, E. Lisi, A. Marrone, A. Melchiorri, and A. Palazzo, *Phys. Rev. D* **104**, 083031 (2021), arXiv:2107.00532 [hep-ph].
- [13] J. M. Berryman and P. Huber, *JHEP* **2101**, 167 (2021), arXiv:2005.01756 [hep-ph].
- [14] C. Giunti, Y. Li, C. Ternes, and Z. Xin, *Phys.Lett.B* **829**, 137054 (2022), arXiv:2110.06820 [hep-ph].
- [15] S. V. Semenov, *Phys. Atom. Nucl.* **83**, 1549 (2020).
- [16] J. N. Bahcall, *Phys. Rev.* **C56**, 3391 (1997), hep-ph/9710491.
- [17] W. C. Haxton, *Phys. Lett.* **B431**, 110 (1998), nucl-th/9804011.
- [18] D. Frekers et al., *Phys. Rev.* **C91**, 034608 (2015).
- [19] J. Kostensalo, J. Suhonen, C. Giunti, and P. C. Srivastava, *Phys.Lett.* **B795**, 542 (2019), arXiv:1906.10980 [nucl-th].
- [20] J. N. Abdurashitov et al. (SAGE), *Phys. Rev.* **C73**, 045805 (2006), nucl-ex/0512041.
- [21] M. Laveder, *Nucl. Phys. Proc. Suppl.* **168**, 344 (2007).
- [22] C. Giunti and M. Laveder, *Mod. Phys. Lett.* **A22**, 2499 (2007), hep-ph/0610352.
- [23] P. Anselmann et al. (GALLEX), *Phys. Lett.* **B342**, 440 (1995).
- [24] W. Hampel et al. (GALLEX), *Phys. Lett.* **B420**, 114 (1998).
- [25] F. Kaether, W. Hampel, G. Heusser, J. Kiko, and T. Kirsten, *Phys. Lett. B* **685**, 47 (2010), arXiv:1001.2731 [hep-ex].
- [26] J. N. Abdurashitov et al. (SAGE), *Phys. Rev. Lett.* **77**, 4708 (1996).
- [27] J. N. Abdurashitov et al. (SAGE), *Phys. Rev.* **C59**, 2246 (1999), hep-ph/9803418.
- [28] J. N. Abdurashitov et al. (SAGE), *Phys. Rev. C* **80**, 015807 (2009), arXiv:0901.2200 [nucl-ex].
- [29] J. M. Berryman, P. Coloma, P. Huber, T. Schwetz, and A. Zhou, *JHEP* **02**, 055 (2022), arXiv:2111.12530 [hep-ph].
- [30] G. Mention et al., *Phys. Rev.* **D83**, 073006 (2011), arXiv:1101.2755 [hep-ex].
- [31] T. A. Mueller et al., *Phys. Rev.* **C83**, 054615 (2011), arXiv:1101.2663 [hep-ex].
- [32] P. Huber, *Phys. Rev.* **C84**, 024617 (2011), arXiv:1106.0687 [hep-ph].
- [33] L. Hayen, J. Kostensalo, N. Severijns, and J. Suhonen, *Phys.Rev.* **C100**, 054323 (2019), arXiv:1908.08302 [nucl-th].
- [34] M. Estienne, M. Fallot, et al., *Phys. Rev. Lett.* **123**, 022502 (2019), arXiv:1904.09358 [nucl-ex].
- [35] V. Kopeikin, M. Skorokhvatov, and O. Titov, *Phys. Rev. D* **104**, L071301 (2021), arXiv:2103.01684 [nucl-ex].
- [36] M. Maltoni and T. Schwetz, *Phys. Rev.* **D68**, 033020 (2003), hep-ph/0304176.
- [37] C. Giunti and M. Laveder, *Phys. Rev.* **D82**, 113009 (2010), arXiv:1008.4750 [hep-ph].
- [38] C. Giunti and C. W. Kim, *Fundamentals of Neutrino Physics and Astrophysics* (Oxford University Press, Oxford, UK, 2007) pp. 1–728.
- [39] I. Alekseev et al. (DANSS), *Phys.Lett.* **B787**, 56 (2018), arXiv:1804.04046 [hep-ex].
- [40] M. Danilov, (2022), talk presented at ICHEP 2022, 41th International Conference on High Energy Physics, 6-13 July 2022, Bologna, Italy.
- [41] J. Ashenfelter et al. (PROSPECT), *Phys.Rev.Lett.* **121**, 251802 (2018), arXiv:1806.02784 [hep-ex].
- [42] M. Andriamirado et al. (PROSPECT), *Phys.Rev.* **D103**, 032001 (2021), arXiv:2006.11210 [hep-ex].
- [43] H. Almazan et al. (STEREO), *Phys.Rev.Lett.* **121**, 161801 (2018), arXiv:1806.02096 [hep-ex].
- [44] H. Almazan Molina et al. (STEREO), *Phys.Rev.* **D102**,

- 052002 (2020), arXiv:1912.06582 [hep-ex].
- [45] Y. Ko *et al.* (NEOS), *Phys.Rev.Lett.* **118**, 121802 (2017), arXiv:1610.05134 [hep-ex].
- [46] Z. Atif *et al.* (RENO, NEOS), *Phys. Rev. D* **105**, L111101 (2022), arXiv:2011.00896 [hep-ex].
- [47] F. An *et al.* (Daya Bay), *Chin.Phys.* **C41**, 013002 (2017), arXiv:1607.05378 [hep-ex].
- [48] S. Gariazzo, C. Giunti, M. Laveder, and Y. F. Li, *JHEP* **1706**, 135 (2017), arXiv:1703.00860 [hep-ph].
- [49] S. Gariazzo, C. Giunti, M. Laveder, and Y. F. Li, *Phys.Lett.* **B782**, 13 (2018), arXiv:1801.06467 [hep-ph].
- [50] C. Giunti, Y. Li, and Y. Zhang, *JHEP* **2005**, 061 (2020), arXiv:1912.12956 [hep-ph].
- [51] C. Giunti, *Phys.Rev.* **D101**, 095025 (2020), arXiv:2004.07577 [hep-ph].
- [52] A. Serebrov *et al.*, *Phys.Rev.D* **104**, 032003 (2021), arXiv:2005.05301 [hep-ex].
- [53] M. Danilov, *J.Phys.Conf.Ser.* **1390**, 012049 (2019), arXiv:1812.04085 [hep-ex].
- [54] M. Andriamirado *et al.* (PROSPECT, STEREO), (2020), arXiv:2006.13147 [hep-ex].
- [55] M. V. Danilov and N. A. Skrobova, *JETP Lett.* **112**, 452 (2020).
- [56] C. Giunti, Y. F. Li, C. A. Ternes, and Y. Y. Zhang, *Phys. Lett. B* **816**, 136214 (2021), arXiv:2101.06785 [hep-ph].
- [57] B. Achkar *et al.* (Bugey), *Nucl. Phys.* **B434**, 503 (1995).
- [58] M. Agostini and B. Neumair, *Eur.Phys.J.* **C80**, 750 (2020), arXiv:1906.11854 [hep-ex].
- [59] P. Coloma, P. Huber, and T. Schwetz, *Eur.Phys.J.* **C81**, 2 (2021), arXiv:2008.06083 [hep-ph].
- [60] M. Aker *et al.* (KATRIN), *Nature Phys.* **18**, 160 (2022), arXiv:2105.08533 [hep-ex].
- [61] M. Aker *et al.* (KATRIN), *Phys. Rev. Lett.* **126**, 091803 (2021), arXiv:2011.05087 [hep-ex].
- [62] M. Aker *et al.* (KATRIN), *Phys.Rev.D* **105**, 072004 (2022), arXiv:2201.11593 [hep-ex].
- [63] A. Saenz, S. Jonsell, and P. Froelich, *Phys. Rev. Lett.* **84**, 242 (2000).
- [64] E. G. Myers, A. Wagner, H. Kracke, and B. A. Wesson, *Phys. Rev. Lett.* **114**, 013003 (2015).
- [65] E. Fermi, *Nuovo Cim.* **11**, 1 (1934).
- [66] J. A. Formaggio, A. L. C. de Gouvea, and R. G. H. Robertson, *Phys.Rept.* **914**, 1 (2021), arXiv:2102.00594 [nucl-ex].
- [67] C. Kraus, A. Singer, K. Valerius, and C. Weinheimer, *Eur.Phys.J.* **C73**, 2323 (2013), arXiv:1210.4194 [hep-ex].
- [68] A. Belesev, A. Berlev, E. Geraskin, A. Golubev, N. Likhovid, *et al.*, *JETP Lett.* **97**, 67 (2013), arXiv:1211.7193 [hep-ex].
- [69] A. Belesev *et al.*, *J. Phys.* **G41**, 015001 (2014), arXiv:1307.5687 [hep-ex].
- [70] C. Giunti, M. Laveder, Y. F. Li, and H. Long, *Phys. Rev.* **D87**, 013004 (2013), arXiv:1212.3805 [hep-ph].
- [71] P. Zyla *et al.* (Particle Data Group), *PTEP* **2020**, 083C01 (2020).
- [72] G. Barenboim, C. A. Ternes, and M. A. Tórtola, *JHEP* **07**, 155 (2020), arXiv:2005.05975 [hep-ph].
- [73] C. Giunti and Y. F. Li, *Phys. Rev. D* **80**, 113007 (2009), arXiv:0910.5856 [hep-ph].
- [74] C. Giunti, M. Laveder, Y. F. Li, Q. Y. Liu, and H. W. Long, *Phys. Rev. D* **86**, 113014 (2012), arXiv:1210.5715 [hep-ph].
- [75] A. Palazzo, *Phys. Rev. D* **83**, 113013 (2011), arXiv:1105.1705 [hep-ph].
- [76] A. Palazzo, *Phys. Rev. D* **85**, 077301 (2012), arXiv:1201.4280 [hep-ph].
- [77] K. Goldhagen, M. Maltoni, S. E. Reichard, and T. Schwetz, *Eur. Phys. J. C* **82**, 116 (2022), arXiv:2109.14898 [hep-ph].
- [78] M. Dentler, A. Hernández-Cabezudo, J. Kopp, P. A. N. Machado, M. Maltoni, I. Martínez-Soler, and T. Schwetz, *JHEP* **08**, 010 (2018), arXiv:1803.10661 [hep-ph].
- [79] B. T. Cleveland, T. Daily, R. Davis, Jr., J. R. Distel, K. Lande, C. K. Lee, P. S. Wildenhain, and J. Ullman, *Astrophys. J.* **496**, 505 (1998).
- [80] B. Aharmim *et al.* (SNO), *Phys. Rev. C* **88**, 025501 (2013), arXiv:1109.0763 [nucl-ex].
- [81] J. Hosaka *et al.* (Super-Kamiokande), *Phys. Rev. D* **73**, 112001 (2006), arXiv:hep-ex/0508053.
- [82] J. P. Cravens *et al.* (Super-Kamiokande), *Phys. Rev. D* **78**, 032002 (2008), arXiv:0803.4312 [hep-ex].
- [83] K. Abe *et al.* (Super-Kamiokande), *Phys. Rev. D* **83**, 052010 (2011), arXiv:1010.0118 [hep-ex].
- [84] G. Bellini *et al.*, *Phys. Rev. Lett.* **107**, 141302 (2011), arXiv:1104.1816 [hep-ex].
- [85] G. Bellini *et al.* (Borexino), *Phys. Rev. D* **82**, 033006 (2010), arXiv:0808.2868 [astro-ph].
- [86] G. Bellini *et al.* (BOREXINO), *Nature* **512**, 383 (2014).
- [87] F. Dydak *et al.*, *Phys. Lett. B* **134**, 281 (1984).
- [88] K. B. M. Mahn *et al.* (SciBooNE, MiniBooNE), *Phys. Rev. D* **85**, 032007 (2012), arXiv:1106.5685 [hep-ex].
- [89] K. Abe *et al.* (Super-Kamiokande), *Phys. Rev. D* **91**, 052019 (2015), arXiv:1410.2008 [hep-ex].
- [90] M. G. Aartsen *et al.* (IceCube), *Phys. Rev. Lett.* **125**, 141801 (2020), arXiv:2005.12942 [hep-ex].
- [91] P. Adamson *et al.* (MINOS), *Phys. Rev. Lett.* **107**, 011802 (2011), arXiv:1104.3922 [hep-ex].
- [92] P. Adamson *et al.* (NOvA), *Phys. Rev. D* **96**, 072006 (2017), arXiv:1706.04592 [hep-ex].
- [93] A. Gando *et al.* (KamLAND), *Phys. Rev. D* **88**, 033001 (2013), arXiv:1303.4667 [hep-ex].
- [94] F. Vissani, *Nucl. Phys. Atom. Energy* **18**, 303 (2017), arXiv:1709.05813 [hep-ph].
- [95] G. Barenboim and J. Lykken, *Phys. Lett.* **B554**, 73 (2003), hep-ph/0210411.